Cell

Programmed ribosomal frameshifting triggers translational stress to promote viral replication

Graphical abstract

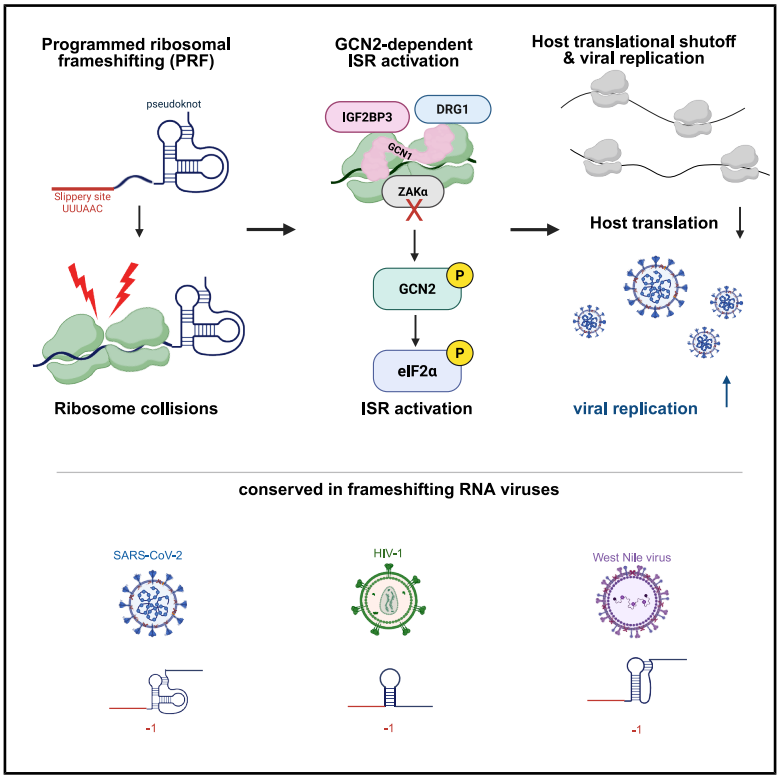

Highlights

- Programmed ribosomal frameshifting acts as a viral stress signal that activates GCN2
- PRF-induced ribosome collisions trigger a non-canonical integrated stress response
- IGF2BP3 and DRG1 couple collided ribosomes to GCN2 independently of ZAKα
- The conserved PRF-GCN2 axis rewires host translation to enhance RNA virus replication

Authors

Audrey Xavier, Melinda Kolling, Ashley M. Bourke, ..., Raul Andino, Sandra Ciesek, Ivan Dikic

Correspondence

dikic@biochem2.uni-frankfurt.de

In brief

Viruses such as SARS-CoV-2 can use programmed ribosomal frameshifting to turn off host translation and promote viral replication, expanding the known uses of programmed ribosomal frameshifting by viruses.

Xavier et al., 2026, Cell *189*, 1–18
November 25, 2026
https://doi.org/10.1016/j.cell.2026.08.031

CellPress

Cell

CellPress
OPEN ACCESS

Article

Programmed ribosomal frameshifting triggers translational stress to promote viral replication

Audrey Xavier,[1,2,19] Melinda Kolling,[3,19] Ashley M. Bourke,[4] Thorsten Mosler,[1] Cristian Prieto-Garcia,[1,5,6] Emil Karaulanov,[17] Michaela Reissland,[7] Michel Tassetto,[8] Damian Kim,[15] Katleen Klaassen,[3] Katharina Grikscheit,[3] Emma Torbica,[3] Verena Dederer,[2] Jonas Busam,[18] Rubina Kazi,[1] Ruth Olmer,[9] Srinivas Reddy Pallerla,[3] Sebastian Mathea,[2] Markus E. Diefenbacher,[12,13,14] Kathi Zarnack,[2,18] Denisa Bojkova,[3] Marek Widera,[3] Ranen Aviner,[15] Raul Andino,[8] Sandra Ciesek,[3,10,11] and Ivan Dikic[1,2,16,20,*]

[1]Institute of Biochemistry II, Faculty of Medicine, Goethe University Frankfurt, Frankfurt am Main, Germany
[2]Buchmann Institute for Molecular Life Sciences, Goethe University, Frankfurt am Main, Germany
[3]Institute for Medical Virology, University Hospital Frankfurt, Goethe University Frankfurt, 60596 Frankfurt am Main, Germany
[4]Max Planck Institute for Brain Research, Frankfurt, Germany
[5]Instituto de Biomedicina de Sevilla (IBiS), Hospital Universitario Virgen del Rocío/CSIC/Universidad de Sevilla), Seville, Spain
[6]Departamento de Biología Celular, Facultad de Biología, Universidad de Sevilla, Seville, Spain
[7]Department of Genome Regulation, Max Planck Institute for Molecular Genetics, Berlin, Germany
[8]Department of Microbiology and Immunology, University of California, San Francisco, 600 16th Street, Room S572E, Box 2280, San Francisco, CA, USA
[9]Leibniz Research Laboratories for Biotechnology and Artificial Organs (LEBAO), Department of Cardiothoracic, Transplantation and Vascular Surgery (HTTG), REBIRTH-Research Center for Translational Regenerative Medicine, Biomedical Research in Endstage and Obstructive Lung Disease Hannover (BREATH), German Center for Lung Research (DZL), Hannover Medical School, Hannover, Germany
[10]Fraunhofer Institute for Translational Medicine and Pharmacology (ITMP), 60596 Frankfurt am Main, Germany
[11]German Center for Infection Research, DZIF, External Partner Site Frankfurt, Frankfurt, Germany
[12]Comprehensive Pneumology Center (CPC), Institute of Lung Health and Immunity (LHI), Helmholtz Munich, Munich, Germany
[13]Ludwig-Maximilian-Universität München (LMU), Munich, Germany
[14]German Cancer Consortium (DKTK), LMU, Munich, Germany
[15]Chan Zuckerberg Biohub, San Francisco, San Francisco, CA, USA
[16]Max Planck Institute of Biophysics, Frankfurt, Germany
[17]Institute of Molecular Biology (IMB), Mainz, Germany
[18]Theodor Boveri Institute, Julius Maximilians University Würzburg, Biocenter, Am Hubland, 97074 Würzburg, Germany
[19]These authors contributed equally
[20]Lead contact
*Correspondence: dikic@biochem2.uni-frankfurt.de
https://doi.org/10.1016/j.cell.2026.08.031

SUMMARY

Programmed ribosomal frameshifting (PRF) is a conserved viral strategy for expressing polyproteins from compact genomes. Although PRF is traditionally viewed as a structural mechanism, here we show that it functions as a regulatory signal that rewires host translation in favor of viral replication. A minimal SARS-CoV-2 PRF element is sufficient to activate the GCN2 arm of the integrated stress response (ISR) independently of the canonical ISR sensor ZAKα. This activation serves as a temporal switch during early infection to shut off host translation and is required for viral propagation in cells and human airway organoids. Proteomic and genetic screens identify DRG1 and IGF2BP3 as key mediators of PRF-induced GCN2 activation. We further show that this PRF-GCN2 axis is conserved in human immunodeficiency virus (HIV)-1 and West Nile virus, highlighting its broad relevance across RNA viruses. These findings reveal a sophisticated mechanism of viral translational control, highlighting PRF as a stress-inducing module that enhances viral replication.

INTRODUCTION

Programmed ribosomal frameshifting (PRF) is a translational mechanism that enables the regulated expression of two overlapping open reading frames (ORFs) within a single mRNA through a one-nucleotide frameshift during translation.[1,2] This strategy is widely conserved among RNA viruses, including coronaviruses,[3–5] influenza A virus (IAV), and human immunodeficiency virus (HIV).[6–8] PRF is typically mediated by a complex, secondary RNA structure such as a pseudoknot,[9–12] a spacer, and a nearby uracil-adenosyl-rich slippery site,[13–15] which together promote ribosomal slippage into an alternative reading frame. Although PRF is often described as a genome-compacting feature or a means to fine-tune the stoichiometry of viral

Please cite this article in press as: Xavier et al., Programmed ribosomal frameshifting triggers translational stress to promote viral replication, Cell (2026), https://doi.org/10.1016/j.cell.2026.08.031

proteins,[16–20] these explanations do not fully account for its evolutionary conservation. A largely unexplored possibility is that PRF actively modulates host cell physiology to favor viral propagation.

Recent structural and biochemical studies in SARS-CoV-2 have shown that pseudoknot-mediated PRF causes ribosomal stalling near the frameshift site,[12] a phenomenon linked to ribosome collisions. These collisions are emerging as key triggers of the integrated stress response (ISR), a signaling network that modulates translation, gene expression, and cell fate in response to diverse stresses.[21–25] Ribosome collisions can be sensed by proteins such as general control nonderepressible 1 (GCN1), GCN20, and ZAKα, which, in turn, activate the eukaryotic translation initiation factor 2A (eIF2α) kinase GCN2.[21] Under amino acid deprivation, ribosomes are stalled by an uncharged tRNA binding to the ribosomal A-site. The resulting ribosome collision interface recruits and activates GCN2 through the interaction of its histidyl-tRNA synthetase (HisRS) domain with the ribosomal P-stalk and GCN1, leading to eIF2α phosphorylation and global translation attenuation.[21,26–28]

Although coronavirus infection is known to engage the ISR, this has primarily been attributed to PERK (in response to endoplasmic reticulum [ER] stress)[29] or PKR (in response to viral double-stranded RNA [dsRNA]).[30–32] The extent of GCN2 activation and whether PRF is involved in this process remains poorly understood.

RNA viruses broadly reprogram the host translatome by targeting signaling pathways such as mTORC1, altering the translation initiation complex, or inducing stress responses.[33–35] In coronaviruses, the viral protein Nsp1 has been implicated as the dominant factor in host shutoff by inserting into the ribosomal mRNA entry tunnel and promoting degradation of host transcripts.[36–39] Viral mRNAs evade this shutdown via a protective 5′ leader sequence. However, additional mechanisms contributing to translational control during SARS-CoV-2 infection are likely but remain insufficiently characterized.

Given the well-established biophysical mechanism of PRF and the growing recognition that ribosome collisions can initiate cellular stress signaling, we hypothesized that PRF-induced ribosome collisions during viral translation activate the ISR. Activation of the ISR suppresses host protein synthesis, thereby creating conditions that ultimately favor viral replication. In this view, SARS-CoV-2 and other PRF-utilizing viruses may exploit PRF not only to regulate the expression of their own proteins but also as a deliberate strategy to disrupt host cell physiology through translational stress pathways.

RESULTS

PRF of SARS-CoV-2 induces a discrete transcriptional and signaling response

Inside the SARS-CoV-2 genome, the frameshifting site lies between ORF1a (covering Nsp1-Nsp11) and ORF1b (covering Nsp12-Nsp16). To test whether PRF triggers a cellular response, we built a dual-luminescence reporter (Renilla/Firefly) measuring frameshift efficiency based on a previous study.[12] A loop1 deletion control (ΔL1) disrupted the pseudoknot structure and significantly reduced frameshifting efficiency compared with the wild-type (WT) construct (FS) (Figure 1A).

To investigate the hypothesis that PRF induces cellular stress, we transiently transfected HEK293T cells with FS and profiled the cellular transcriptome by RNA sequencing (RNA-seq), comparing FS-transfected cells to ΔL1, mock-transfected, and non-transfected (NT) controls. Principal-component analysis (PCA) and sample correlation clustering showed that FS and ΔL1 samples clustered together and apart from NT and mock conditions (Figures S1A and S1B), indicating that transfection of either construct drives a marked transcriptional shift beyond that caused by the transfection procedure alone. DESeq2 analysis identified a robust differential gene expression signature in FS-transfected cells, not only relative to mock and NT controls but also when compared with the ΔL1 control (Table S1). Hierarchical clustering of the 382 differentially expressed genes (DEGs) found in FS versus ΔL1 revealed that although a subset of genes was upregulated in FS-transfected cells in comparison to all control conditions, a distinct cohort of transcripts was downregulated specifically in the FS versus ΔL1 comparison, suggesting that the ΔL1 construct itself induces a distinct gene expression signature (Figure 1B). Interestingly, gene set enrichment analysis (GSEA) revealed that FS alone partially mimics authentic SARS-CoV-2 infection signaling (Figure S1C; Table S1) and upregulates pathways that converge in translational stress (hypoxia, nuclear factor κB [NF-κB], p53, and UV damage).[40–43] Conversely, downregulated pathways were primarily enriched for cell cycle progression and unfolded protein response (UPR) signatures (Figures S1D–S1F). Complementing these findings, DRUG-seqr analysis further linked the FS profile to translation inhibitors such as harringtonine and emetine (Figure 1C). Taken together, these results prompted us to examine whether the ISR pathway is activated upon FS transfection, using ΔL1 as a stringent control.

Confirming RNA-seq results, at the protein level, FS specifically activated the ISR—as evidenced by elevated activated transcription factor 4 (ATF4) and phosphorylated eIF2α (Figure 1D)—without inducing other stress pathways such as ATF6a (as indicated by cleavage and processed levels) or XBP1 (as measured by the level of its active splicing variant) (Figures 1D and 1E). This ISR activation was confirmed across multiple cell lines (Huh7 and Caco2) using a fluorescence-activated cell sorting (FACS)-sorted dual-fluorescence reporter (mCherry/GFP) (Figure S2A). Subsequent western blotting confirmed the activation of the ISR pathway by FS in both Huh7 and Caco2 cell lines (Figure S2B).

eIF2α can be phosphorylated by 4 different kinases, namely GCN2, PERK, PKR, and heme-regulated inhibitor (HRI).[44] Mechanistically, knocking down or pharmacologically inhibiting (via A92) the kinase GCN2—but not PERK, PKR, or HRI—rescued eIF2α phosphorylation and ATF4 levels (Figures 1F and 1G) without altering frameshifting efficiency itself (Figure 1H). To exclude differences in mRNA levels between FS and ΔL1 in the cytosol that could result from plasmid transfection, we also directly transfected each FS and ΔL1 transcript alone, which mirrored the results of plasmid transfection (Figure S2C). Furthermore, pull-down of the FS RNA transcript using the MS2CP system[45] showed association of endogenous GCN2

Please cite this article in press as: Xavier et al., Programmed ribosomal frameshifting triggers translational stress to promote viral replication, Cell (2026), https://doi.org/10.1016/j.cell.2026.08.031

CellPress
OPEN ACCESS

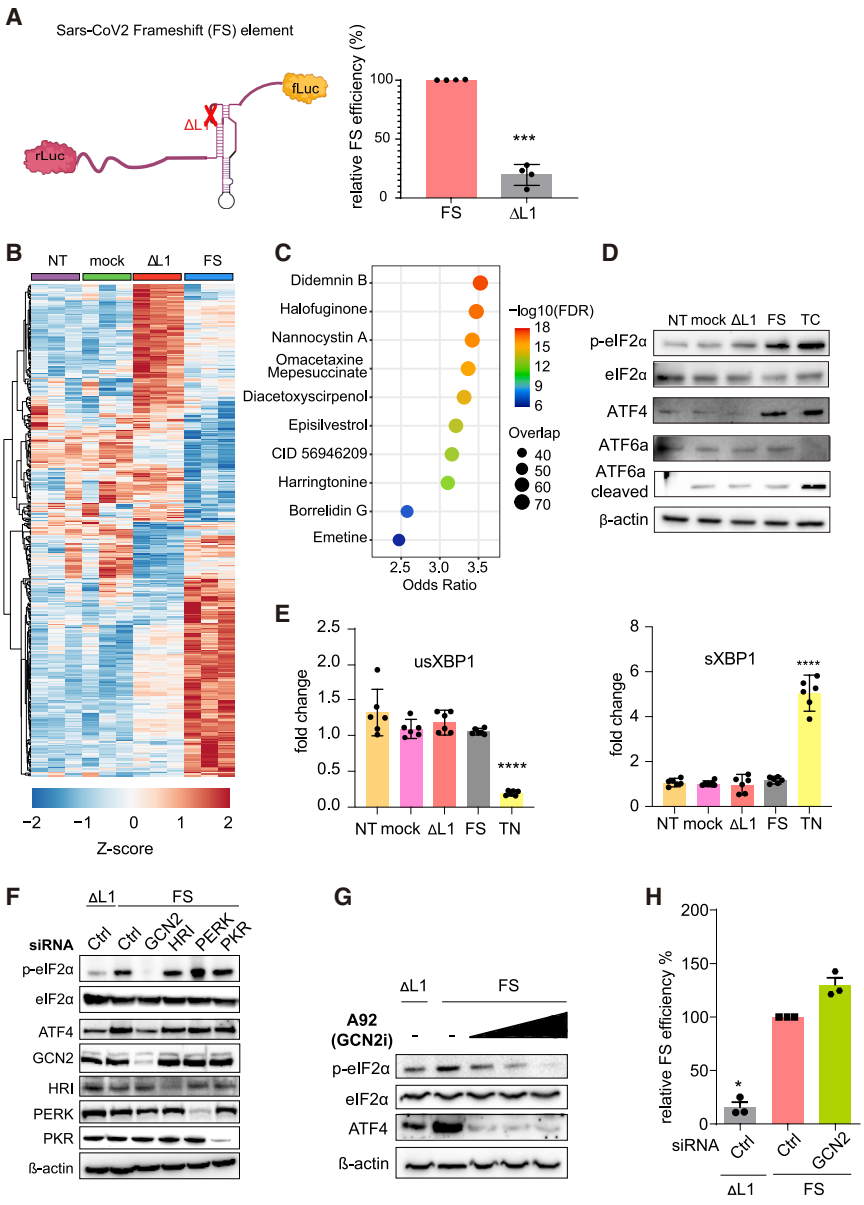

Figure 1. PRF alone generates a distinct transcriptional and signaling response

(A) Left, schematic representation of the frameshifting construct (FS), with the site deleted in the ΔL1 mutant indicated in red. Right, relative FS efficiency normalized to the SARS-CoV-2 readthrough construct (IFC). Error bars indicate SD. Significance was determined by paired *t* test. *** $p < 0.001$ ($n = 4$).

(B) Gene expression heatmap of the 382 DEGs found in the FS versus ΔL1 differential expression comparison (Table S1), showing their relative levels (*Z* scores) in all 12 analyzed samples of HEK293T cells, which were either non-transfected (NT), mock transfected, or transfected with ΔL1 or FS expression constructs ($n = 3$).

(C) Bubble plot of top mimetic drugs linked to translation inhibition generated via DRUG-seqr enrichment analysis using the 197 FS versus ΔL1 upregulated DEGs. See also Figure S1 and Table S1.

(D) Western blot analysis of cellular stress markers. HEK293T cells were transfected with ΔL1, FS, or mock control for 48 h or treated with 2 μg/mL tunicamycin (TC) for 4 h. See also Figure S2.

(E) qPCR analysis of fold changes in spliced (sXBP1) or unspliced XBP1 (usXBP1) upon transfection with ΔL1 or FS constructs for 48 h or treatment with 50 nM thapsigargin (TN) for 6 h ($n = 6$). Error bars indicate SD. Significance was determined by one-way ANOVA and Dunnett's post hoc test. **** $p < 0.0001$.

(F) Western blot analysis of ΔL1- and FS-transfected HEK cells with concomitant knockdown of stress kinases.

(G) HEK cells were treated with GCN2 inhibitor A92 at 0.5, 1, and 2 μM, 6 h prior to transfection with ΔL1 or FS constructs. Lysates were analyzed by western blotting.

(H) Relative frameshift efficiency of ΔL1- and FS-transfected HEK cells that were treated with scrambled control (ctrl) or GCN2 siRNA. Error bars indicate SEM. Significance was determined by one-way ANOVA followed by Dunnetts's post hoc test. * $p < 0.05$ ($n = 3$). Part of this figure was created using BioRender.

with the FS transcript but not with the ΔL1 transcript (Figure S3A). We also probed the association between GCN2 and FS RNA by immunoprecipitating transfected GCN2, followed by detection of RNA via RT-qPCR. The results showed that full-length GCN2 and the HisRS domain associate with the FS transcript, whereas the catalytic domain failed to associate (Figures S3B and S3C). Altogether, the minimal pseudoknot sequence of SARS-CoV-2 alone is sufficient to elicit a distinct transcriptional and specific ISR signaling response in host cells.

SARS-CoV-2 infection induces an early-stage GCN2-dependent ISR activation

Although previous studies showed that the isolated frameshifting sequence induces cellular stress upon transfection,[30,32,46,47] whether authentic SARS-CoV-2 infection activates GCN2 remained unclear. Unlike passive stress pathways triggered by viral component overload (e.g., PKR or PERK-mediated ER stress), GCN2 may directly sense PRF early in infection before viral products accumulate. However, GCN2 activation in response to viral PRF has not been explored. To investigate this, we infected Calu3 cells with SARS-CoV-2. Infection elicited a time-dependent, multilayered ISR initiated by GCN2. At multiplicity of infection (MOI) 1, eIF2α phosphorylation exhibited a biphasic pattern: a mild early phase and a stronger late phase. GCN2 was activated as early as 2 h post-infection (hpi), strictly coinciding with the onset of viral PRF (measured by Nsp12 expression) and immediate eIF2α phosphorylation/ATF4 induction (Figures 2A and 2B). In contrast, PKR and PERK activation occurred much later, at 10 and 24 hpi, respectively (Figure 2B). Lower viral loads (MOI 0.02) altered overall kinetics, but GCN2

Please cite this article in press as: Xavier et al., Programmed ribosomal frameshifting triggers translational stress to promote viral replication, Cell (2026), https://doi.org/10.1016/j.cell.2026.08.031

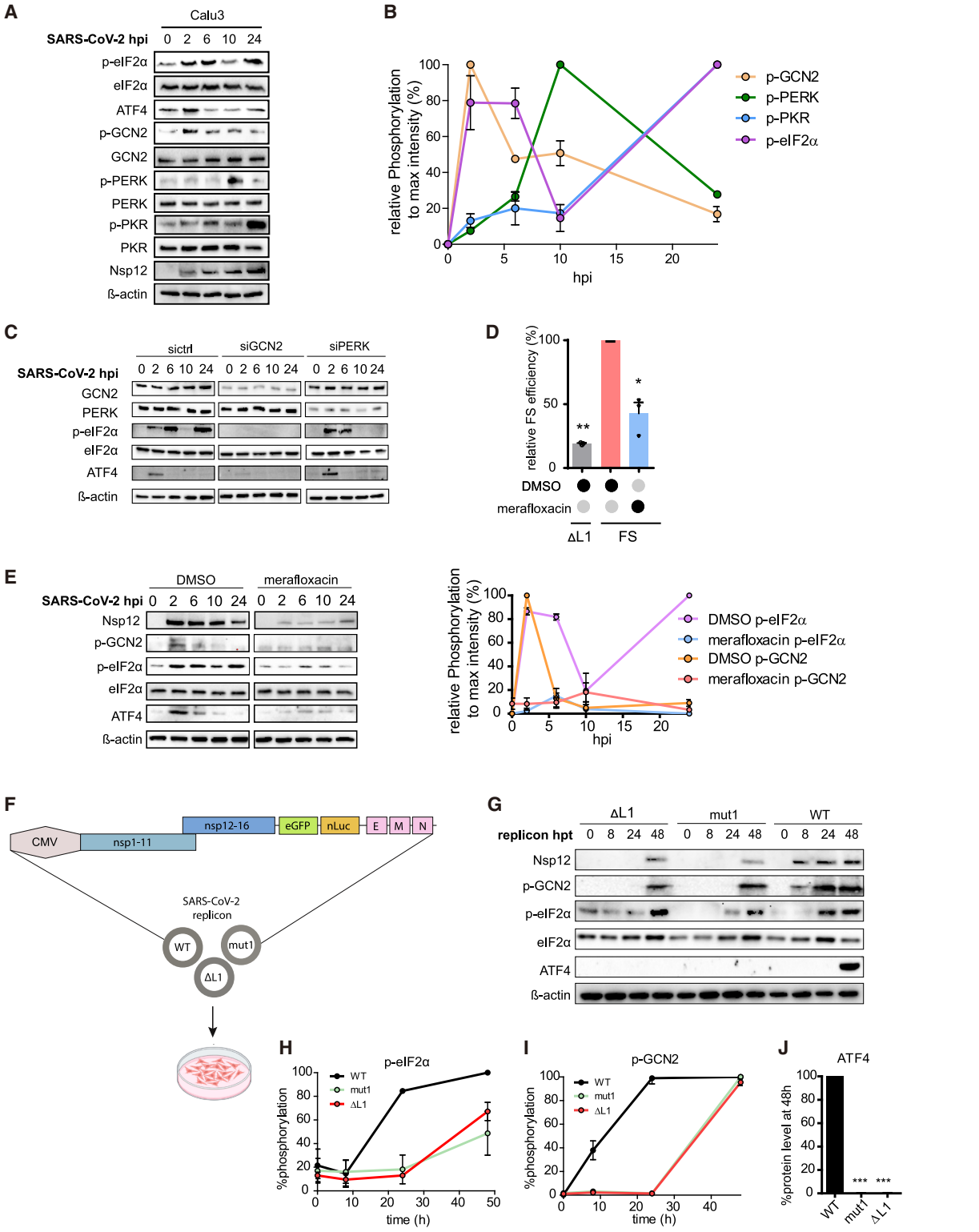

Figure 2. SARS-CoV-2 infection leads early GCN2-mediated ISR activation

(A) Calu3 cells were infected with SARS-CoV-2 at MOI 1, and samples were prepared at 0, 2, 6, 10, and 24 h post-infection, followed by western blotting analysis. (B) Quantification of time-dependent phosphorylation status of GCN2, PERK, eIF2α, and PKR during SARS-CoV-2 infection based on western blot results ($n = 2$). Phosphorylation values were normalized to the highest values for each protein, respectively. Error bars indicate SD.

(legend continued on next page)

Please cite this article in press as: Xavier et al., Programmed ribosomal frameshifting triggers translational stress to promote viral replication, Cell (2026), https://doi.org/10.1016/j.cell.2026.08.031

activation consistently preceded PERK and PKR. Consistently, knockdown or pharmacological inhibition (via A92) of GCN2 reduced early-stage eIF2α phosphorylation, whereas PERK knockdown selectively diminished late-stage phosphorylation (Figures 2C, S4A, and S4B). This indicates that SARS-CoV-2 infection induces a time-dependent, multilayered ISR response that is initiated by GCN2.

Accordingly, SARS-CoV-2 infection induced GCN2-mediated ISR in air-liquid interface (ALI) cultures of primary human bronchial epithelial (HBE) cells, and treatment with A92 attenuated ISR activation (Figures S4C and S4D). To establish causality between viral PRF and GCN2-ISR activation, we employed two complementary strategies. First, we treated SARS-CoV-2-infected cells with the frameshifting inhibitor merafloxacin.[12] We confirmed the reduction of frameshifting efficiency using our minimal reporter system (Figure 2D). In agreement, treatment with merafloxacin abolished ISR induction in response to SARS-CoV-2 infection (Figures 2E, S4E, and S4F).

Second, using a SARS-CoV-2 replicon system, we introduced the pseudoknot-disrupting mutation, ΔL1, and mutations in the ribosome-interacting residues (mut1; G13486C and C13487T) (Figure 2F). Based on a structural study,[12] the ribosome directly interacts with the nucleotide G13486, enhancing ribosome stalling at the pseudoknot. Both mutants significantly reduced frameshifting efficiency, replication activity, and GCN2/eIF2α/ATF4 signaling compared with the WT replicon (Figures S5A and S5B). ΔL1 was more active in replication compared with mut1, possibly because the two nucleotide mutations in mut1 result in an alanine-to-leucine substitution, which might compromise the function of Nsp12, the RNA-dependent RNA polymerase of SARS-CoV-2. In contrast, the deletion of three nucleotides in ΔL1 (T13485, G13486, and C13487) does not disrupt Nsp12 function. Transfection of the replicon indicated delayed expression of ORF1b protein Nsp12 compared with SARS-CoV-2-infected cells. This delay is likely caused by the lack of structural proteins that package the viral genome during infection and are known to help initiate viral expression (e.g., nucleocapsid).[48] Although delayed by transfection, the WT SARS-CoV-2 replicon recapitulated the GCN2, eIF2α, and ATF4 dynamics seen with clinical isolates of SARS-CoV-2. In contrast, these responses were weaker with the mut1 and ΔL1 replicon (Figures 2G–2I), especially with ATF4 induction being blunted (Figures 2G and 2J).

Because PRF mutations also alter protein stoichiometry and inherently lower viral fitness,[49] we tested whether suppressed ISR signaling was simply a passive consequence of decreased viral replication. Ectopic, doxycycline-inducible expression of ATF4—the key downstream effector of GCN2—restored replication in the ΔL1 replicon in a dose-dependent manner. If reduced ISR were merely a result of lower replication, ATF4 overexpression should not rescue viral replication. Instead, we observed that forced ATF4 expression restored ΔL1 replicon replication in a dose-dependent manner (Figure S5C), suggesting that ATF4 itself actively promotes viral replication. The mut1 replicon also showed a partial increase, although this was not statistically significant—likely due to impaired Nsp12 functionality from coding mutations (Figure S5D). Altogether, PRF leads to early GCN2-dependent ISR activation. These findings support a direct role for PRF-induced ISR signaling, and specifically ATF4, in enhancing SARS-CoV-2 replication.

GCN2 is required for SARS-CoV-2 replication

To investigate how activation of GCN2 affects the progress of SARS-CoV-2 infection, we treated Calu3 cells with A92 during infection. A92 strongly reduced SARS-CoV-2 viral replication in a dose-dependent manner (Figures 3A and 3B). The effect of GCN2 inhibition was recapitulated across different SARS-CoV-2 variants, namely Delta, Omicron BA.1, and JN.1 (Figures S6A–S6C), and in ALI HBE cultures (Figure S6D). We further confirmed the pro-viral role of GCN2 via small interfering RNA (siRNA)-mediated depletion of GCN2 in Calu3 cells (Figure 3C).

SARS-CoV-2 infection leads to translational shutoff of host genes, while translation of viral genes continues to surge. GCN2-mediated ISR is associated with translational shutoff, while extremely high levels of ISR lead to cell death.[21,38] Hence, we hypothesized that, in addition to the known Nsp1-mediated mechanisms, SARS-CoV-2 may rearrange the host translational landscape by fine-tuning the ISR through PRF. To investigate this hypothesis, we explored the changes in ribosomal profiles

(C) Calu3 cells were transfected with ctrl, GCN2, and PERK siRNA and infected with SARS-CoV-2 at MOI 1. Samples for western blotting were prepared at 2, 6, 10, and 24 h post-infection ($n = 2$).
(D) Relative frameshift efficiency in HEK cells treated with DMSO or merafloxacin (20 μM) and transfected with ΔL1 or FS constructs ($n = 3$). Error bars indicate SD. Significance was determined using one-way ANOVA followed by Dunnetts's post hoc test. $^{*}p < 0.05$, $^{**}p < 0.01$.
(E) Western blot analysis of ISR markers in Calu3 cells after treatment with DMSO or merafloxacin and infection with SARS-CoV-2 at MOI 1 for 2, 6, 10, and 24 h. Western blot quantification of time-dependent phosphorylation status of GCN2 and eIF2α during SARS-CoV-2 infection, with or without merafloxacin treatment (20 μM). Phosphorylation values of eIF2α and GCN2 of merafloxacin-treated cells were normalized to the highest levels of the proteins in DMSO-treated cells ($n = 3$). Error bars indicate SD. See also Figure S4.
(F) Schematic representation of the SARS-CoV-2 replicon plasmid system containing the entire SARS-CoV-2 genome except the spike gene, which is replaced by nano-luciferase (nLuc) and enhanced green fluorescent protein (EGFP).
(G) Western blot analysis of ISR markers in HEK cells transfected with SARS-CoV-2 WT, mut1, or ΔL1 replicons for 8, 24, and 48 h.
(H) Western blot quantification of time-dependent phosphorylation status of p-eIF2α upon WT, ΔL1, and mut1 replicon transfection. Phosphorylation values of mutants were normalized to the highest levels of the WT ($n = 3$). Error bars indicate SD.
(I) Western blot quantification of time-dependent phosphorylation status of p-GCN2 upon WT, ΔL1, and mut1 replicon transfection. Phosphorylation values of mutants were normalized to the highest levels of the WT ($n = 3$). Error bars indicate SD.
(J) Western blot quantification of ATF4 protein level upon WT, ΔL1, and mut1 replicon transfection. Protein values of mutants were normalized to the highest levels of the WT ($n = 3$). Significance was determined using one-way ANOVA followed by Dunnett's post hoc test. $^{***}p < 0.001$ ($n = 3$). Part of this figure was created using BioRender.
See also Figure S5.

Please cite this article in press as: Xavier et al., Programmed ribosomal frameshifting triggers translational stress to promote viral replication, Cell (2026), https://doi.org/10.1016/j.cell.2026.08.031

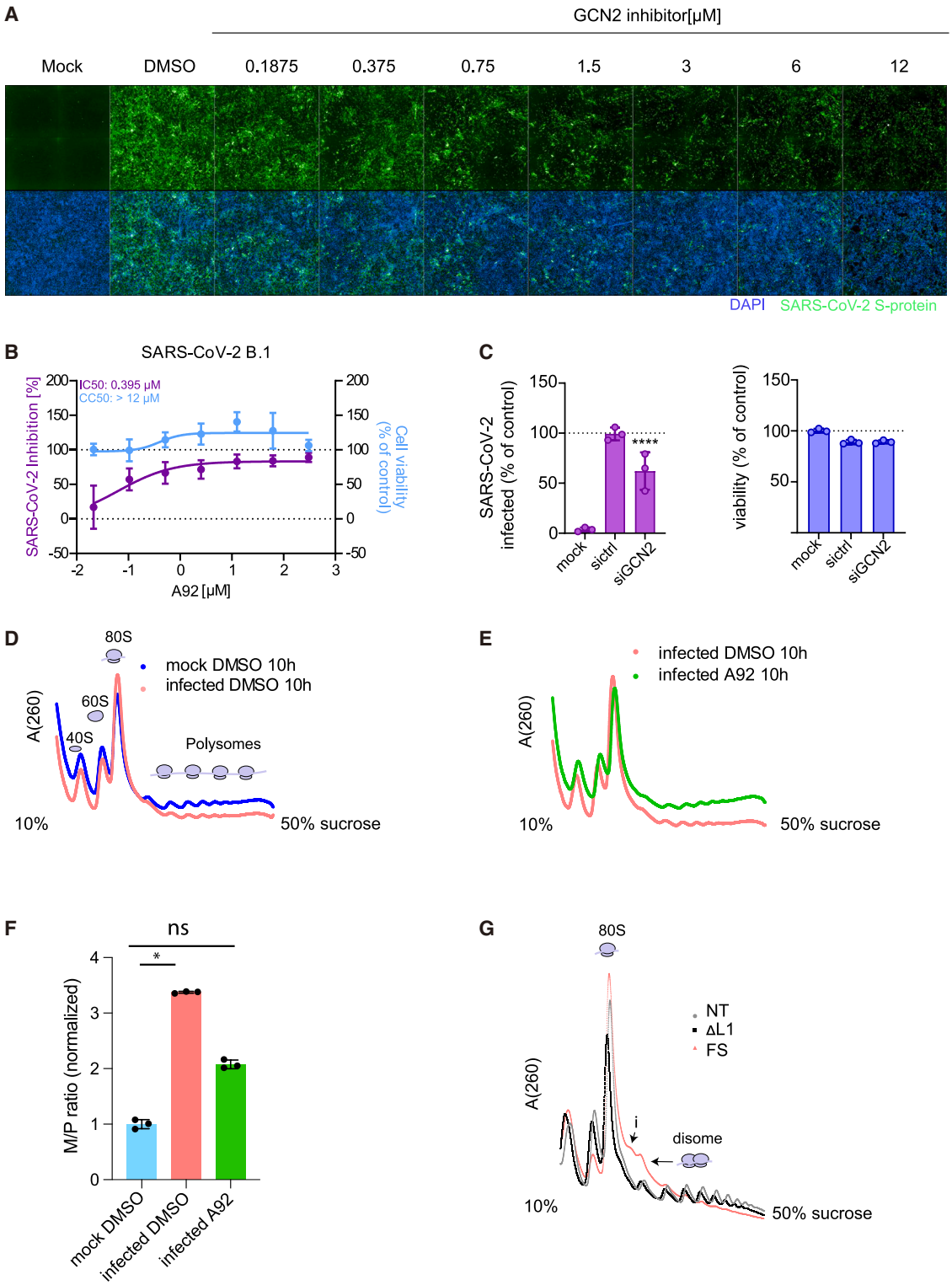

Figure 3. SARS-CoV-2 replication and host ribosome remodeling are GCN2 dependent

(A) Fluorescence microscopy images of Calu3 cells treated with increasing doses of A92 and infected with SARS-CoV-2 at MOI 0.02 for 24 h. SARS-CoV-2 S protein was stained in green and DAPI in blue. Scale bar represents 500 μm.

(B) Quantification of (A) and determination of IC50 (purple) and CC50 (blue) (A92 concentrations plotted on a $\log_{10}$ scale) (n = 3). Error bars indicate SD.

(legend continued on next page)

Please cite this article in press as: Xavier et al., Programmed ribosomal frameshifting triggers translational stress to promote viral replication, Cell (2026), https://doi.org/10.1016/j.cell.2026.08.031

during infection and in the presence of A92 using polysome profiling. Compared with non-infected cells that contain a large portion of translating polysomes, SARS-CoV-2 infection led to a reduction in overall cellular translation in a time- and viral-load-dependent manner, as evidenced by a marked shift in most ribosomes from polysomes to monosomes (Figures 3D and S7). At MOI 1, SARS-CoV-2 infection reduces the translational capacity of the cell over time, with little effect at 4 hpi (Figure S7A), a moderate effect at 10 hpi (Figure 3D), and full translational shutoff at 24 hpi (Figure S7C). Interestingly, A92 slightly rescued translational defects at 4 hpi (Figure S7B) and largely rescued them at 10 hpi (Figures 3E and 3F). This is in accordance with the early timing of GCN2-mediated ISR activation and its capacity to cause early translational shutoff. At 24 hpi, orthogonal pathways mediated by PKR and PERK lead to eIF2α phosphorylation and late-phase translational shutoff (Figure S7C), and A92 treatment shows no effect (Figure S7D). Another likely explanation is that Nsp1-mediated translational shutoff remains unaffected by changes in the ISR. We also confirmed the effect of A92 in rescuing translational shutoff at lower MOI, which was assayed at 24 hpi due to slower viral progression in this condition (Figures S7E–S7G).

We corroborated these findings by performing ribosome-sequencing (Figures S8A–S8E). Read quality, size distribution, and phasing parameters were similar between SARS-CoV-2 viral RNA and host mRNA (Figures S8A–S8D). Like polysome profiling, PCA analysis indicated that treatment with A92 upon infection led to the resumption of an intermediate state between non-infected and infected cells, thus partially restoring homeostatic translational levels (Figure S8D). However, importantly, we observed a strong translational upregulation of ATF4 target genes in SARS-CoV-2-infected versus non-infected cells, indicating ISR-mediated translational shutoff, which was largely negated by A92 treatment (Figure S8E). A puromycin incorporation assay further confirmed the polysome and ribosome profiling results, revealing a full rescue of host cell translation upon A92 treatment at 10 hpi (Figure S8F).

To uncouple Nsp1 from ISR-mediated effects on translational shutoff, we monitored changes in polysome profiles and puromycin incorporation of NT versus ΔL1- and FS-transfected cells. In contrast to NT and ΔL1, FS transfection led to a shift of polysomes to monosomes and lower puromycin incorporation, indicating that FS transfection alone is sufficient to cause modest translational shutoff (Figures 3G and S8G). Although translational shutoff caused by FS was rather modest compared with Nsp1 transfection, co-transfection of both led to synergistic effects comparable to those observed with SARS-CoV-2 infection (Figure S8H). Taken together, SARS-CoV-2 infection changes the host translational landscape in a PRF- and GCN2-dependent manner to favor its own replication.

PRF-mediated GCN2 activation depends on ribosome stalling but is ZAKα independent

Next, we investigated the mechanism by which PRF induces GCN2 activation. In Figure S3, we had shown that GCN2 is associated with the FS transcript. To gain deeper insights, we created different pseudoknot mutants that contained a premature stop codon right before (PreM) or after the pseudoknot (PS), where PreM would lead to the ribosome being stalled in front of, and PS on, the pseudoknot. We also included an in-frame control (IFC) that has a stop codon deletion inside the pseudoknot, as well as a slippery site mutant (SSM) that contains a point mutation in the slippery site (Figure 4A). We confirmed that all mutants were defective in frameshifting except IFC, where the ribosome continued to translate 100% of the firefly luciferase (Figure 4B). As expected, transfection with FS led to GCN2 and eIF2α phosphorylation (Figure 4C). Surprisingly, transfection of SSM and PS yielded ISR activation, whereas ΔL1, PreM, and IFC did not (Figure 4C). This allowed us to deduce that GCN2 activation requires ribosome stalling in proximity to the structurally intact pseudoknot and that the mere presence of pseudoknot structure (PreM) in the cell is insufficient to trigger GCN2 activation. Because ΔL1 and IFC carry a mutation in the pseudoknot, the structural integrity of the secondary RNA structure of the pseudoknot is compromised, leading to less ribosome stalling at the frameshifting site. This accounts for the diminished GCN2 activation with ΔL1 and IFC constructs. To confirm the importance of ribosome stalling at the pseudoknot site, we treated cells with puromycin to dissociate the ribosomes from the RNA over time. We pulled down FS versus ΔL1 RNA and observed GCN2 association with FS RNA specifically, which was reduced over time upon puromycin treatment (Figures 4D and 4E). Ribosome dissociation was confirmed by blotting for 40S subunit protein RPS12 and equal RNA input and immunoprecipitation by RT-qPCR (Figure 4E). Furthermore, we tested whether we could recapitulate ribosome stalling-dependent GCN2 activation in a minimal cell-free *in vitro* translation system derived from rabbit reticulocyte lysate (RRL). The RRL system was supplied with *in vitro*-transcribed FS and ΔL1 RNA and purified GCN2 from insect cells. Rabbit eIF2α was phosphorylated *in vitro* only in the presence of FS RNA and purified GCN2, whereas ΔL1 RNA or the lack of GCN2 showed no eIF2α phosphorylation (Figure 4F). Importantly, pre-treatment with the translation

(C) Percent infected cells and cell viability of SARS-CoV-2-infected Calu3 cells transfected with siRNA control or GCN2 ($n = 3$). Error bars indicate SD. Significance was determined using one-way ANOVA followed by Dunnett's post hoc test. **** $p < 0.0001$. See also Figure S6.

(D) Polysome profile (average of $n = 3$) of Calu3 cells treated with DMSO (blue) and infected with SARS-CoV-2 (red) for 10 h at MOI 1.

(E) Polysome profile (average of $n = 3$) of Calu3 cells treated with A92 at 3μM and infected with SARS-CoV-2 for 10 h at MOI 1 (green), and polysome profile of Calu3 cells infected with SARS-CoV-2 for 10 h at MOI 1 and treated with DMSO (red). See also Figure S7.

(F) Quantification of monosome-to-polysome (M/P) ratio for all three conditions ($n = 3$). Significance was determined using a non-parametric test (Kruskal-Wallis). Error bars indicate SD.

(G) Polysome profile (average of $n = 2$) of HEK293T cells NT (gray) or transfected with ΔL1 (black) or FS (red). Monosome and disome fractions are indicated, as well as a halfmer peak (i) between monosome and disome. Error bars indicate SD; *$p < 0.05$. Part of this figure was created using BioRender.

See also Figures S8 and S9.

Please cite this article in press as: Xavier et al., Programmed ribosomal frameshifting triggers translational stress to promote viral replication, Cell (2026), https://doi.org/10.1016/j.cell.2026.08.031

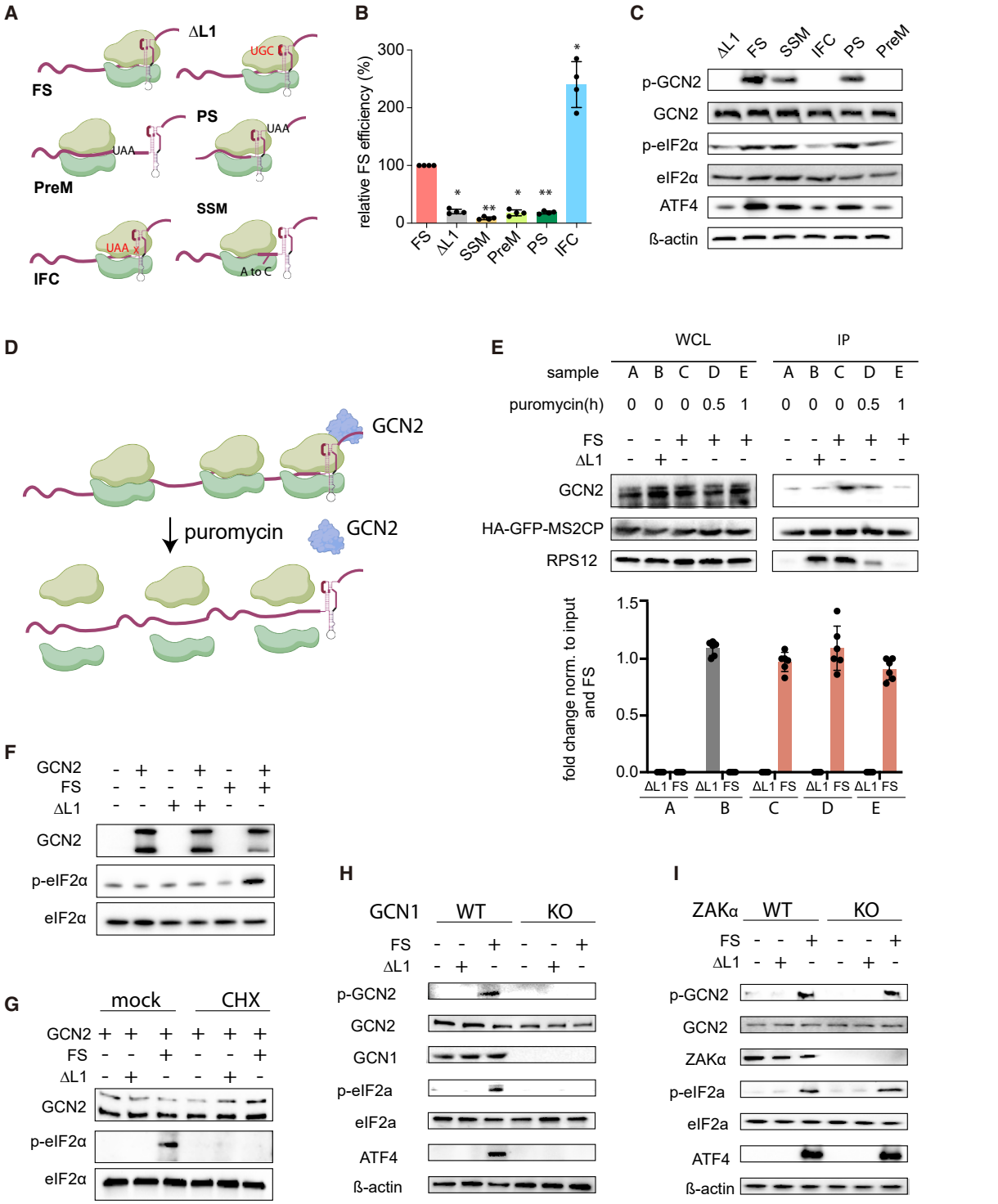

Figure 4. Mechanistic insights into GCN2 activation by PRF

(A) Schematic representation of different SARS-CoV-2 FS constructs, with expected ribosome positions during translation. This image was made using BioRender.

(B) Frameshift efficiencies relative to WT SARS-CoV-2 FS of HEK cells transfected with ΔL1, FS, PreM (premature stop codon before pseudoknot, nt 13,429, GenBank ID OX300254.1), PS (pseudostop, stop codon after pseudoknot, nt 13,545, GenBank ID OX300254.1), IFC (in-frame control), and SSM (slippery site mutant) constructs. Error bars indicate SD. Significance was determined by one-way ANOVA followed by Dunnett's post hoc test. $^{**}p < 0.01$, $^{*}p < 0.05$ ($n = 4$).

(C) HEK cells were transfected with ΔL1, FS, PreM, PS, IFC, and SSM constructs. ISR activation was analyzed via western blotting.

(legend continued on next page)

Please cite this article in press as: Xavier et al., Programmed ribosomal frameshifting triggers translational stress to promote viral replication, Cell (2026), https://doi.org/10.1016/j.cell.2026.08.031

elongation inhibitor cycloheximide (CHX) abolished eIF2α phosphorylation in the presence of FS RNA in this cell-free system, indicating that active translation is required for ISR activation (Figure 4G). Overall, these data indicate that GCN2 activation requires the ribosome to reach the pseudoknot and likely requires additional ribosome-associated factors for its full activation.

Previous studies have indicated that ribosome collision leads to GCN2 activation through the leucine zipper kinase ZAKα and the adapter protein GCN1.[21,50–53] Although GCN1 was required for GCN2 activation, to our surprise, ZAKα was dispensable for ISR activation induced by FS transfection (Figures 4H and 4I), and FS neither led to ZAKα phosphorylation nor activated the stress-activated protein kinase (SAPK) (JNK/p38) pro-apoptotic signaling pathways that are downstream of ZAKα (Figures S9A and S9B).

As GCN2 activation was dependent on GCN1 but independent of ZAKα, we examined whether FS causes ribosome collisions *in cellulo*. We transfected cells with ΔL1 or FS constructs, treated cellular lysates with RNase I, and monitored disome accumulation via polysome profiling. Although polysome fractions in NT- and ΔL1-transfected cells collapsed into monosomes and free ribosome subunits, FS-transfected cells accumulated nuclease-resistant disomes (Figure S9C). RT-qPCR with primers specific to the published ribosome collision site[12] showed a 60-fold increase in FS RNA compared with ΔL1 in the disome fraction, confirming that disome accumulation occurs on the intact frameshifting site (Figure S9D). Of note, we also observed the accumulation of an additional ribosome species intermediate (1) between monosomes and disomes upon FS transfection and polysome profiling, which remained as a shoulder of the disome peak upon nuclease digestion (Figures 3G and S9C). This observation indicates dynamic changes between monosomes and disomes, quality control intermediates, and scanning 40S complexes that could play a role in ZAKα-independent cellular signaling. Taken together, ribosome collision activates the ISR during SARS-CoV-2-mediated ribosomal frameshifting in a GCN1-dependent and ZAKα-independent manner.

PRF-mediated ISR activation is IGF2BP3 and DRG1 dependent

As PRF-mediated ISR activation is independent of ZAKα, we explored whether other factors could be involved in the activation of GCN2. To this end, we performed an MS2CP pull-down of FS versus ΔL1 RNA and analyzed associated factors via mass spectrometry. This identified 35 proteins that were significantly enriched in FS RNA over ΔL1 (cut-off of −log10(0.05)) (Figure 5A). We next performed a siRNA-mediated knockdown screen of proteins that associated more with FS RNA and assessed their requirement in PRF-mediated ISR activation by monitoring eIF2α phosphorylation. Knockdown of IGF2BP3, PSMD7, PSMC5, UPF1, and DRG1 reproducibly reduced eIF2α phosphorylation levels compared with scrambled siRNA (Figure 5B). PSMD7 and PSMC5 depletion led to high cellular toxicity, and thus we excluded them from further studies. Loss of UPF1 led to a significant reduction in frameshift efficiency and was consequently excluded as an upstream activator of ISR (Figure 5C). Left with two factors, DRG1 and IGF2BP3, we first confirmed their relevance for SARS-CoV-2 infection. Like GCN2, knockdown of DRG1 and IGF2BP3 resulted in reduced SARS-CoV-2 replication, indicating that both factors are required for SARS-CoV-2 replication and may thus be involved in the ISR pathway (Figure 5D).

Focusing further on IGF2BP3 and DRG1, we reproduced the binding of these factors to FS RNA via pull-down and western blotting (Figure 5E). Although depletion of DRG1 did not affect GCN2 association with FS RNA, knockdown of IGF2BP3 clearly abolished this interaction (Figures 5F and 5G), suggesting that IGF2BP3 and DRG1 operate in two successive steps during GCN2 activation by PRF.

We next asked whether the involvement of IGF2BP3 and DRG1 is specific to PRF or common to other ISR cues. To address this, we used a well-established response to the peptidyl transferase inhibitor anisomycin, which acts as an antibiotic that inhibits protein translation.[54] When applied at intermediate concentrations, ANS leads to the stalling and collision of ribosomes in a controlled manner, which triggers the activation of GCN2 via ZAKα and GCN1.[21] At higher concentrations, ribosomes are all halted immediately, and no collision occurs. Consistent with this notion, we observed eIF2α phosphorylation at 1 mg/L ANS, whereas lower or higher concentrations failed to activate the ISR pathway. Treatment with the GCN2 inhibitor A92 attenuated ISR activation in response to intermediate ANS concentrations, confirming that eIF2α phosphorylation occurs through GCN2 (Figure S10A). As expected, knockdown of ZAKα attenuated eIF2α phosphorylation in response to ANS treatment (Figure 5H). Interestingly, knockdown of IGF2BP3 similarly abrogated ISR activation, whereas knockdown of DRG1 did not have an effect (Figures 5H and 5I). Other general cues, such as UV treatment or glutamine starvation, displayed a similar trend, with ISR activation being dependent on IGF2BP3 (Figures S10B and

(D) Schematic representation of ribosomal translation with and without puromycin treatment over time. As translation is inhibited by puromycin, ribosomes and GCN2 dissociate from the FS RNA. This image was made using BioRender.
(E) Cells co-transfected with GFP-MS2CP and ΔL1 or FS constructs and treated with puromycin (100 μg/ml) for 0, 30, or 60 min. ΔL1 or FS RNA coimmunoprecipitation (coIP) was analyzed via western blotting for GCN2. Equal pull-down of ΔL1 and FS RNA was verified via qPCR with a shared primer for both constructs. Fold change was normalized to input and FS RNA. Error bars indicate SD. Significance was determined by one-way ANOVA followed by Dunnett's post hoc test ($n = 6$).
(F) *In vitro* kinase assay with GCN2 purified from insect cells and *in vitro*-transcribed ΔL1 or FS RNA in RRL. Rabbit eIF2α phosphorylation was detected via western blotting.
(G) *In vitro* kinase assay with GCN2 purified from insect cells and *in vitro*-transcribed ΔL1 or FS RNA in RRL. RRL was pre-treated or untreated with 100 mg/L CHX prior to adding other components. Rabbit eIF2α phosphorylation was detected via western blotting ($n = 2$).
(H) Western blot analysis of WT or GCN1 knockout (KO) cells transfected with ΔL1 or FS RNA ($n = 2$).
(I) Western blot analysis of WT or ZAKα KO cells transfected with ΔL1 or FS RNA. See also Figure S9. Part of this figure was created using BioRender.

Please cite this article in press as: Xavier et al., Programmed ribosomal frameshifting triggers translational stress to promote viral replication, Cell (2026), https://doi.org/10.1016/j.cell.2026.08.031

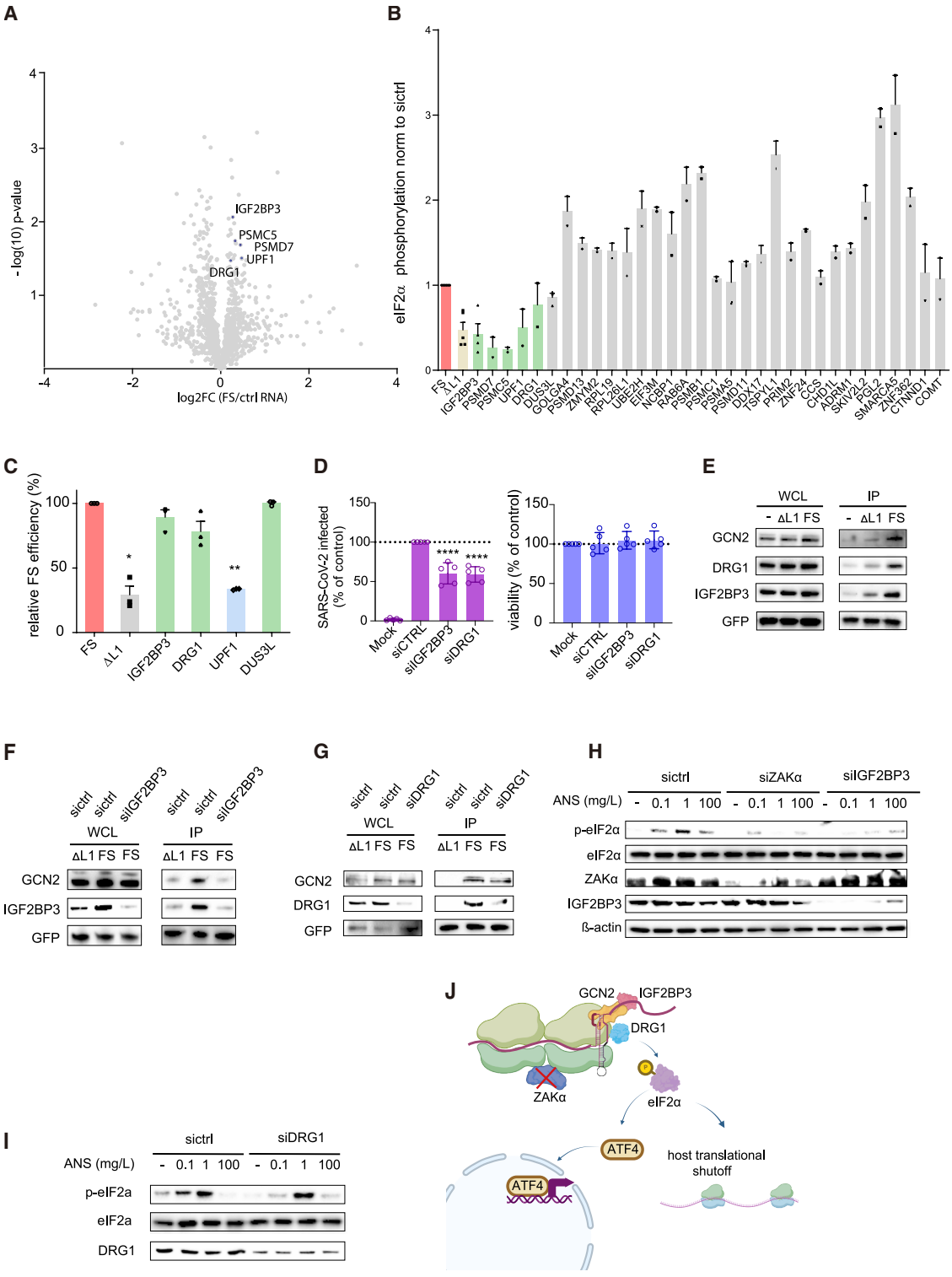

Figure 5. PRF mediates ISR activation and is IGF2BP3 and DRG1 dependent

(A) Mass spectrometry analysis of GFP-MS2CP-mediated pull-down of ΔL1 or FS RNA. Binders that are important for eIF2α phosphorylation are highlighted in purple (n = 3).

(B) siRNA screen of candidates associated with FS RNA. eIF2α phosphorylation was assessed via western blotting in response to FS transfection during knockdown of candidate genes. Results were quantified from two independent experiments, and genes showing a reduction in eIF2α phosphorylation are highlighted in green. Error bars indicate SD.

(legend continued on next page)

Please cite this article in press as: Xavier et al., Programmed ribosomal frameshifting triggers translational stress to promote viral replication, Cell (2026), https://doi.org/10.1016/j.cell.2026.08.031

S10C) but independent of DRG1 (Figures S10D and S10E). In summary, we identified two factors that are necessary for PRF-mediated GCN2 activation, with IGF2BP3 being required for general ribosome collision sensing by recruiting GCN2 to the collision site and DRG1 being specifically mandatory for PRF-mediated ISR activation independent of GCN2 recruitment (Figure 5J).

GCN2 is activated by ribosome stalling during HIV and WNV infection

Many other RNA viruses also exhibit complex RNA secondary structures, in which ribosomes are stalled and PRF occurs.[7,55,56] Thus, we explored whether HIV-1 and West Nile virus (WNV) could also exploit the ISR in their favor. Notably, early infection with HIV-1 has been shown to induce GCN2-ATF4 signaling, which enhances virus replication,[57] although the exact mechanism of this activation has not been elucidated. Confirming previous reports, infection of Jurkat cells with HIV-1 revealed GCN2 and eIF2α phosphorylation at 24 hpi, followed by ATF4 activation at 48 hpi, which were attenuated by A92 treatment during infection (Figure 6A). ISR activation correlated well with the timing of frameshifting, as indicated by the accumulation of HIV-1 p15 protein, a cleaved intermediate of p55 (Figure 6A), which is cleaved by a HIV-1 protease that is only translated upon frameshifting. Similar to SARS-CoV-2, A92 treatment impaired HIV-1 replication (Figures 6B and 6C). Accordingly, we designed minimal frameshifting constructs of HIV-1 with the WT frameshifting sequence, an IFC, and an SSM. To disrupt ribosome stalling, we deleted the stem loop structure altogether (ΔSL) (Figure 6D). Like SARS-CoV-2, the minimal FS sequence of HIV-1 (Figure 6E) activated the GCN2-mediated ISR. Again, although SSM and IFC do not frameshift (Figure 6E), both constructs led to pathway activation (Figure 6F). For HIV-1, IFC mutations were not contained in the RNA sequence comprising the stem loop and thus do not affect its structural integrity. In contrast, ISR activation for the ribosome-stalling-incompetent ΔSL was clearly diminished (Figure 6F). These results establish PRF as the mechanism by which the GCN2-ATF4 axis is activated upon HIV-1 infection.

WNV infection of ARPE-19 cells exhibited similar ISR activation dynamics as SARS-CoV-2 (Figure S11A), with early activation of GCN2 starting from 2 hpi (Figures S11A and S11B), whereas PERK and PKR are only activated at 10 and 24 hpi, respectively. Simultaneous treatment with A92 led to a reduction of early eIF2α phosphorylation and ATF4 protein levels (Figure 6G) and significantly reduced WNV replication in a dose-dependent manner (Figures 6H and S11C). Most importantly, WNV FS minimal construct, IFC, and SSM led to ISR activation (Figures 6I–6K), which was abolished in pseudoknot deletion construct (ΔPK) (Figure 6K). Again, in contrast to SARS-CoV-2 IFC, WNV IFC does not contain mutations in the pseudoknot sequence. At last, we confirmed whether IGF2BP3 and DRG1 were also required for HIV and WNV replication. Surprisingly, both factors share conserved functions among frameshifting RNA viruses (Figures S11D and S11E). Taken together, we conclude that the PRF-GCN2 pathway and its benefit in viral replication is a shared strategy among other frameshifting RNA viruses.

DISCUSSION

PRF is traditionally thought to expand viral coding capacity and balance viral protein stoichiometry. However, our findings show that it also directly reprograms host translation. Minimal PRF elements from SARS-CoV-2, HIV-1, and WNV cause ribosome collisions that engage the GCN2 kinase via its GCN1/HisRS interaction at the exposed ribosome P-stalk, triggering eIF2α phosphorylation and global host translational repression. Rather than serving purely as an antiviral defense, early GCN2-mediated ISR activation actively benefits viral replication. Mild early ISR dampens host gene expression without inducing cell death, whereas late-stage ISR—dominated by PERK and PKR—antagonizes replication. Our data suggest a temporal switch in ISR function, with early GCN2-mediated signaling aiding viral replication and late-stage ISR, mediated by inactive GCN2 and active PERK or PKR, acting in opposition. This model aligns with reports that frameshifting viruses, such as coronaviruses, HIV, and hepatitis C, deploy mechanisms to counteract PKR and GCN2 activation at later stages.[57–60] Viruses appear to exploit this temporal switch: early GCN2 activation fuels replication, whereas downstream eIF2α dephosphorylation (via PP1-GADD34)[60–64] or viral counteraction mechanisms help reinitiate viral protein synthesis before PERK and PKR dominate. A similar mechanism for SARS-CoV-2 could explain the biphasic pattern of eIF2α phosphorylation observed in the course of infection.

The PRF-GCN2 pathway acts synergistically with SARS-CoV-2 Nsp1 to execute host translational shutoff while maintaining alternative translation programs essential for viral propagation and cell survival.[39,65] Downstream GCN2 effectors such as ATF4 help sustain non-canonical translation initiation even amid global host repression.[65] Viruses have evolved multiple mechanisms to reinitiate translation during host translational shutoff. Vesicular stomatitis virus deactivates eIF2α-mediated translation, while favorably modifying the eIF4F complex to specifically promote viral protein synthesis.[33] Further studies are

(C) Relative frameshift efficiency of HEK cells transfected with control, IGF2BP3, DRG1, and UPF1 siRNA and ΔL1 or FS constructs. Significance was determined using one-way ANOVA followed by Dunnett's post hoc test ($n = 3$). *$p < 0.05$, **$p < 0.01$. Error bars indicate SD.
(D) Percent infected area and cell viability of SARS-CoV-2-infected Calu3 cells, transfected with siRNA control, siIGF2BP3, and siDRG1 ($n = 3$). Error bars indicate SD. Significance was determined by one-way ANOVA followed by Dunnetts's post hoc test ($n = 5$).
(E) MS2CP coIP of ΔL1 or FS RNA analyzed via western blotting ($n = 2$).
(F) MS2CP coIP of ΔL1 or FS RNA in the context of IGF2BP3 siRNA analyzed via western blotting ($n = 2$).
(G) MS2CP coIP of ΔL1 or FS RNA in the context of DRG1 siRNA control analyzed via western blotting ($n = 2$).
(H) Western blot analysis of HEK cells transfected with control, Zakα, or IGF2BP3 siRNA and treated with anisomycin at indicated concentrations ($n = 2$).
(I) Western blot analysis of HEK cells transfected with control or DRG1 siRNA and treated with anisomycin at the indicated concentrations ($n = 2$).
(J) Graphical description of the working model of PRF-mediated GCN2 activation. GCN2 is recruited to the stalled ribosome via IGF2BP3 in the presence of DRG1. This image was made using BioRender. See also Figure S10.

Please cite this article in press as: Xavier et al., Programmed ribosomal frameshifting triggers translational stress to promote viral replication, Cell (2026), https://doi.org/10.1016/j.cell.2026.08.031

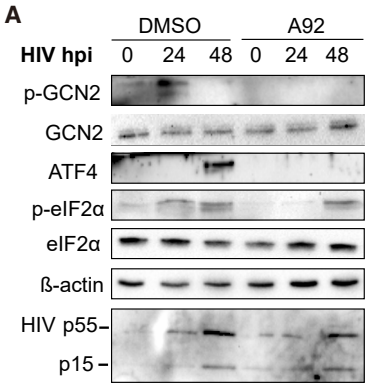

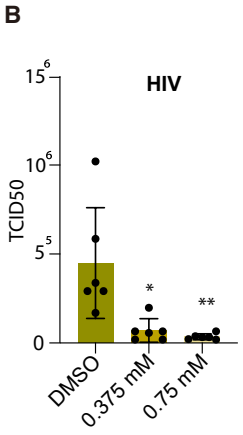

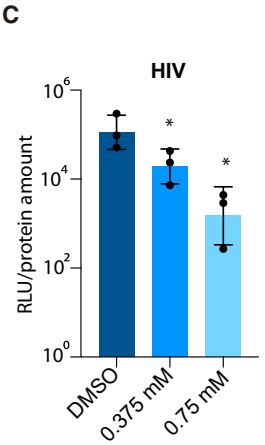

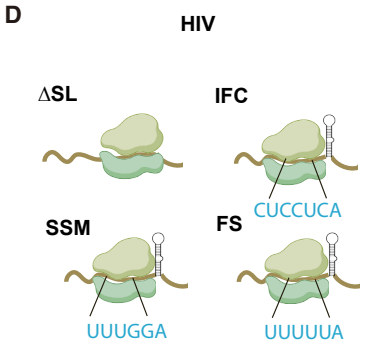

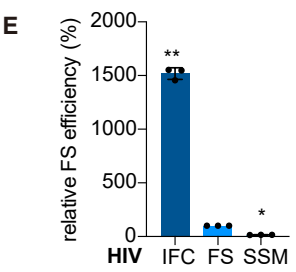

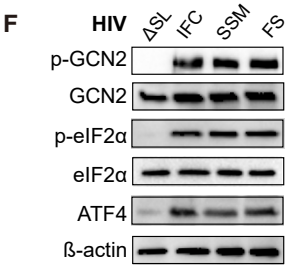

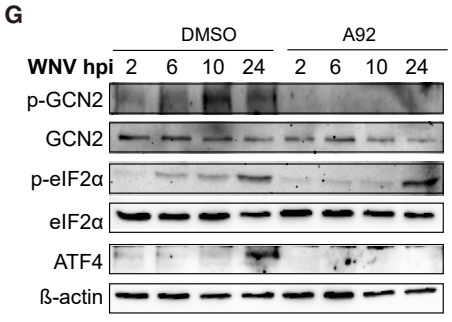

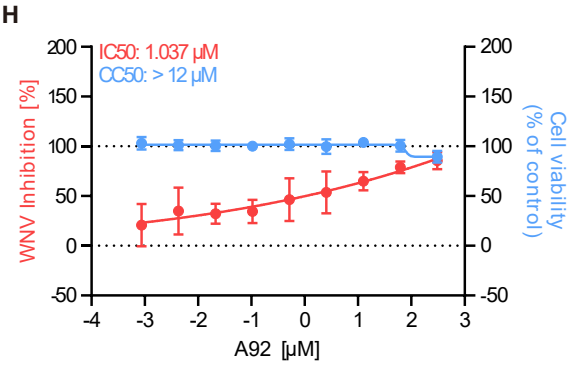

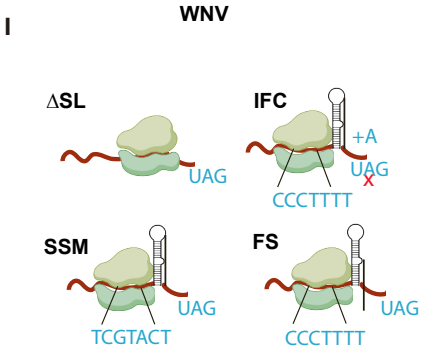

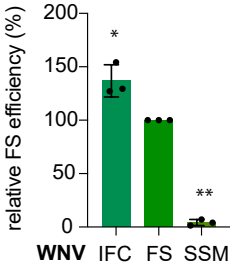

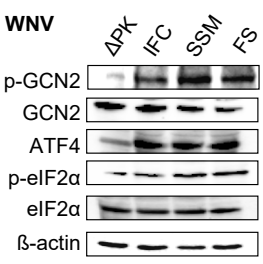

(legend on next page)

Please cite this article in press as: Xavier et al., Programmed ribosomal frameshifting triggers translational stress to promote viral replication, Cell (2026), https://doi.org/10.1016/j.cell.2026.08.031

required to elucidate the exact mechanism of viral translation initiation during SARS-CoV-2 infection.

Although PRF is essential for coronavirus and retrovirus replication, flaviviruses from the Japanese encephalitis virus (JEV) serogroup use frameshifting for expression of accessory proteins, which are non-essential for replication. This includes WNV or JEV, in which expression of the accessory protein NS1′ is associated with elevated virulence and neuroinvasion.[66] The literature on the ISR in WNV infection is limited, and there are discrepancies based on the viral strain used. The highly pathogenic WNV NY99 strain used in this study was shown to induce eIF2α phosphorylation[67] and host translational shutdown.[68] Herein, we demonstrated that WNV uses GCN2-dependent early ISR activation to fuel its replication. Further studies are required to evaluate the importance of the GCN2-ISR axis in other frameshifting viruses.

Ribosome collisions are increasingly recognized as triggers of cellular stress responses, particularly through the GCN1/GCN2 signaling axis.[69,70] Ultimately, PRF-dependent ISR activation is also triggered by ribosome collisions, and is clearly dependent on GCN2 recruitment to the collision site by GCN1. Thus, our mechanistic data indicating an association of the GCN2 HisRS domain with the intact frameshifting construct are based on the exposed ribosome P-stalk of the collided ribosome. This notion is further supported by the requirement for a translating ribosome on the frameshifting RNA for GCN2 activation. However, other factors involved in collision sensing remain poorly understood. Although bacterial infections have been shown to employ ribosome collisions to activate ZAKα-dependent signaling for their own benefit, we found viral PRF-dependent ribosome collision sensing to be independent of ZAKα.[71,72] Although some studies have detected ribosome stalling, ribosome profiling studies of cells infected with SARS-CoV-2, including our own data, failed to detect ribosome collisions at the PRF site *in cellulo*.[65,73–76] However, similar to experiments in RRL, polysome profiling reveals an accumulation of disomes and free 40S subunits upon PRF expression, pointing to distinct ribosome quality control (RQC) dynamics.[12,77]

Mutations disrupting the pseudoknot or stem loop abrogate GCN2 activation, underscoring the necessity of structured RNA in ISR induction. Mutation of the slippery site did not influence ISR activation, although prolonged ribosome pausing might be expected.[12] Furthermore, SARS-CoV-2, WNV, and HIV differ in their stimulatory elements. This may indicate that although pausing and collision is required, the exact duration may not affect ISR activation per se but perhaps rather determine downstream cell fate decisions. However, at this point, we cannot exclude the possibility that additional factors, such as the state of ribosomal rotation or modulation of helicase activity, may also regulate ISR activity. It is increasingly evident that different types of mRNA lesions, including poly(A) tracts, premature stop codons, or truncations, elicit diverse ribosome behaviors and stress responses.[21,50,78–80] The exact mechanism that defines the pathways activated in response to different mRNA traits remains enigmatic but may be determined by the number of stalled or collided ribosomes within the cell, the period of stalling (short or extended), or distinct conformations of stalled or collided ribosomes, which represent distinct binding surfaces for a variety of sensing factors.

Through unbiased proteomic and siRNA screens, we identified IGF2BP3 and DRG1 as mediators of GCN2 activation in the context of PRF. IGF2BP3, an m^{6}A-binding protein previously known to stabilize transcripts and modulate stress responses, appears to recruit GCN2 to frameshifting RNA elements.[81] Recent studies show that m^{6}A plays a role in inducing ribosome pausing and collision,[82] which may lead to mRNA degradation through YTHDF2-mediated pathways.[83] Intriguingly, IGF2BP3 is known to shelter and stabilize mRNA in stress granules, protecting it from degradation,[81] which could indicate that not all ribosome collision pathways lead to mRNA degradation. IGF2BP3 was required for GCN2 activation independent of the activating trigger, suggesting a role parallel to that of ZAKα. DRG1, a translation-associated GTPase, has been implicated in ribosome collision sensing in yeast.[77] Curiously, DRG1 was dispensable for GCN2 activation during anisomycin-induced stress and other general cues, yet was essential in the PRF

Figure 6. PRF of HIV-1 and WNV activates GCN2-mediated ISR

(A) Western blot analysis of Jurkat cells infected with HIV-1 NL4-3 and treated with DMSO or A92 at 0.375 μM. Jurkat cells were treated with DMSO, 0.375 μM A92, or 0.75 μM A92.

(B and C) Viral supernatants were used to infect TZM-bl cells and further analyzed via (B) X-gal assay and (C) luciferase assay. At 48 hpi, TZM-bl cells were lysed, and luciferase activity was measured. Relative light units were normalized to the total amount of protein analyzed by Bradford assay. Significance was determined by one-way ANOVA followed by Dunnett's post hoc test; (B) $n = 6$, (C) $n = 3$. $^*p < 0.05$, $^{**}p < 0.01$. Error bars indicate SD.

(D) Schematic representation of HIV-1 minimal frameshifting constructs ΔSL (stem loop deletion), IFC (in-frame control), SSM (slippery site mutant), and FS (HIV-1 WT frameshifting sequence) and expected ribosome occupancy. This image was created with BioRender.

(E) Frameshift efficiency determined by dual-luciferase assay of HIV-1 minimal frameshifting constructs IFC, FS, and SSM. Significance was determined by one-way ANOVA followed by Dunnett's post hoc test ($n = 3$). $^*p < 0.05$, $^{**}p < 0.01$. Error bars indicate SD.

(F) Western blot analysis of ISR markers in HEK cells transfected with ΔSL, IFC, SSM, and FS HIV minimal frameshifting constructs.

(G) ARPE-19 cells were infected with WNV at MOI 1 or infected with WNV and treated with A92 at 3μM, and samples were prepared at 0, 2, 6, 10, and 24 h post-infection, followed by western blotting analysis of ISR markers.

(H) A92 dose-dependent inhibition of WNV, with A92 concentrations plotted on a $\log_{10}$ scale. Error bars indicate SD.

(I) Schematic representation of WNV minimal frameshifting constructs ΔSL (stem loop deletion), IFC, SSM, and FS (WNV WT frameshifting sequence) and expected ribosome occupancy. This image was created with BioRender.

(J) Frameshift efficiency determined by dual-luciferase assay of WNV minimal frameshifting constructs IFC, FS, and SSM. Significance was determined by one-way ANOVA followed by Dunnett's post hoc test ($n = 3$). $^*p < 0.05$, $^{**}p < 0.01$. Error bars indicate SD.

(K) Western blot analysis of ISR markers in HEK cells transfected with ΔPK, IFC, SSM, and FS WNV minimal frameshifting constructs. Part of this figure was created using BioRender.

See also Figure S11.

context across different RNA viruses, suggesting stressor-specific roles in ribosome surveillance.

Collectively, our findings uncover an unappreciated function of PRF as a virus-driven mechanism for inducing translational stress and reprogramming host translation. By activating GCN2 and co-opting ISR signaling, PRF allows viruses to silence host gene expression while promoting their own propagation. These results broaden our understanding of host-virus interactions and open new avenues for targeting viral stress pathways therapeutically.

Limitations of the study

Multiple experiments support our model of PRF-GCN2 in host translational suppression and viral replication, though several limitations exist. First, using a spike-deleted replicon allowed us to assess replication deficits, but plasmid transfection efficiency caused temporal delays in ISR activation compared with authentic infection. Second, because PRF is essential for SARS-CoV-2 replication, completely separating ISR activation from viral replication remains challenging. Third, due to safety regulations, frameshifting mutations were tested in minimal reporter systems rather than in live SARS-CoV-2, HIV-1, or WNV genomes, limiting detailed mechanistic insights during full viral infection—though the concept of PRF-induced ISR was broadly confirmed across cell lines and human airway organoids. Finally, although we identified DRG1 and IGF2BP3 as key factors in the PRF-GCN2 axis, their precise molecular mechanism of GCN2 activation requires future study, alongside testing potential therapeutic interventions in live mouse models.

RESOURCE AVAILABILITY

Lead contact

Further information and requests for resources should be directed to and will be fulfilled by the lead contact, Ivan Dikic (dikic@biochem2.uni-frankfurt.de).

Materials availability

All unique/stable reagents generated in this study are available from the lead contact upon request with a completed materials transfer agreement.

Data and code availability

All data and materials used for this study are available from the lead contact upon reasonable request. RNA-seq data have been deposited in the NCBI Gene Expression Omnibus repository with the dataset identifier GEO: GSE322665. The mass spectrometry proteomics data have been deposited in the ProteomeXchange Consortium via the PRIDE partner repository with the dataset identifier PRIDE: PXD057424.

ACKNOWLEDGMENTS

We thank Glenn Masson from the University of Dundee (MRC), UK, for providing the GCN2 constructs for insect purification, and Julia Weigand from Philipps-University Marburg for fluorescent PRF reporter constructs. We thank Safia Ouazar and Lena Stegmann for technical assistance (Goethe University, Frankfurt). We thank Heiner Schaal for providing plasmid DNA. We thank all members of the Quantitative Proteomics Unit at IBC2 (Goethe University, Frankfurt), in particular Martin Adrian-Allgood for sample preparation and measurements, Kristina Wagner for producing LC columns, and David Krause for help with (bio)informatics. We thank Frankfurt Virus Platform of the Goethe University and University Hospital Frankfurt for providing virus isolates and associated protocols (for further information, contact Denisa Bojkova, Sandra Ciesek, and virussolutions@unimedizin-ffm.de). Frankfurt Virus Solutions is supported by the LOEWE priority program CoroPan. Support by the IMB Genomics Core Facility and the use of its NextSeq2000 is gratefully acknowledged. This work was supported by Clusterproject EnABLE, funded by the Hessian Ministry for Science and Arts, and the CRC project on selective autophagy (project ID: 259130777, SFB1361), funded by the Deutsche Forschungsgemeinschaft (German Research Foundation, DFG) to I.D. The DFG also funded the LC-MS systems (easy nLC 1200, QExactive HF) (project ID: 259130777, SFB1177 – Selective Autophagy; easy nLC1200, Orbitrap Fusion LUMOS) used in this study (FuGG Project ID: 403765277). S.C. was funded by the DFG (project ID: 318346496, SFB1292). The work was in part supported by the DFG priority program SPP1923 (WI 5086/1-1), the Innovation Center TheraNova, and the LOEWE Priority Program CoroPan funded by the Hessian Ministry for Science and Arts (HMWK).

AUTHOR CONTRIBUTIONS

Conceptualization: A.X.; methodology: A.X., M.K., S.C., T.M., R.K., A.M.B., C.P.-G., M.R., M.E.D., J.B., K.Z., M.T., R. Aviner, E.K., V.D., S.M., R.O., D.K., and K.K.; investigation: A.X., M.K., T.M., C.P.-G., M.R., M.T., E.T., K.K., K.G., D.B., and R. Aviner; visualization: A.X., M.K., T.M., A.M.B., C.P.-G., R. Aviner, and E.K.; discussion: A.X., M.K., T.M., C.P.-G., M.T., J.B., K.Z., R. Aviner, R. Andino, E.K., S.C., I.D., S.M., and M.W.; project administration: A.X. and I.D.; funding acquisition: I.D. and S.C.; supervision and leadership: A.X., R. Andino, S.C., and I.D.; writing – original draft: A.X. and I.D.; writing – review & editing: R. Andino, M.K., A.M.B., T.M., C.P.-G., E.K., and I.D.

DECLARATION OF INTERESTS

The authors declare no competing interests.

STAR★METHODS

Detailed methods are provided in the online version of this paper and include the following:

- KEY RESOURCES TABLE
- EXPERIMENTAL MODEL AND STUDY PARTICIPANT DETAILS
  - Cell culture
- METHOD DETAILS
  - Western blotting
  - Cell culture and plasmid/siRNA transfection
  - Frameshift assay by luminescence
  - FACS sorting of cells with or without frameshift
  - Plasmid construction
  - RNA-transfection
  - RNA-Sequencing
  - RT-qPCR
  - Disome RT-qpcr
  - MS2 pulldown assay
  - RIP-qPCR assay
  - In vitro translation and GCN2 kinase assay
  - Puromycin incorporation assay
  - Recombinant protein purification GCN2 insect cell expression and purification
  - Virus propagation and infection
  - Nanopore GridION Sequencing
  - TZM-bl Luc Assay
  - TZM-bl x-Gal Assay
  - Transepithelial electrical resistance (TEER) measurement
  - Antiviral and viability assay
  - Immunofluorescence
  - Detection of extracellular viral RNA
  - siRNA-mediated knockdown
  - Polysome profiling
  - UV-treatment and glutamine starvation
  - Mass spectrometry sample preparation

- Mass spectrometry data acquisition
- Mass spectrometry data analysis
- Ribo-seq
- Ribo-seq analysis
- Generation of SARS-CoV2 replicon reporter system

- QUANTIFICATION AND STATISTICAL ANALYSIS

SUPPLEMENTAL INFORMATION

Supplemental information can be found online at https://doi.org/10.1016/j.cell.2026.08.031.

Received: June 30, 2025
Revised: May 11, 2026
Accepted: August 18, 2026

REFERENCES

1. Alam, S.L., Atkins, J.F., and Gesteland, R.F. (1999). Programmed ribosomal frameshifting: Much ado about knotting!. Proc. Natl. Acad. Sci. USA *96*, 14177–14179. https://doi.org/10.1073/pnas.96.25.14177.
2. Farabaugh, P.J. (1996). Programmed Translational Frameshifting. Microbiol. Rev. *60*, 103–134. https://doi.org/10.1128/mr.60.1.103-134.1996.
3. Brierley, I., Boursnell, M.E.G., Binns, M.M., Bilimoria, B., Blok, V.C., Brown, T.D., and Inglis, J.E. (1987). An efficient ribosomal frame-shifting signal in the polymerase-encoding region of the coronavirus IBV. EMBO J. *6*, 3779–3785.
4. Denison, M.R., Zoltick, P.W., Leibowitz, J.L., Pachuk, C.J., and Weiss, S.R. (1991). Identification of Polypeptides Encoded in Open Reading Frame Ib of the Putative Polymerase Gene of the Murine Coronavirus Mouse Hepatitis Virus A59. J. Virol. *65*, 3076–3082.
5. Herold, J., and Siddell, S.G. (1993). An "elaborated" pseudoknot is required for high frequency frameshifting during translation of HCV 229E polymerase mRNA. Nucleic Acids Res. *21*, 5838–5842. https://doi.org/10.1093/nar/21.25.5838.
6. Falk, H., Mador, N., Udi, R., Panet, A., and Honigman, A. (1993). Two cis-Acting Signals Control Ribosomal Frameshift between Human T-Cell Leukemia Virus Type II gag and pro Genes. J. Virol. *67*, 6273–6277. https://doi.org/10.1128/jvi.67.10.6273-6277.1993.
7. Jacks, T., Power, M.D., Masiarz, F.R., Luciw, P.A., Barr, P.J., and Varmus, H.E. (1988). Characterization of ribosomal frameshifting in HIV-1 gag-pol expression. Nature *331*, 280–283. https://doi.org/10.1038/331280a0.
8. Nam, S.H., Copeland, T.D., Hatanaka, M., and Oroszlan, S. (1993). Characterization of Ribosomal Frameshifting for Expression of pol Gene Products of Human T-Cell Leukemia Virus Type I. J. Virol. *67*, 196–203. https://doi.org/10.1128/jvi.67.1.196-203.1993.
9. Brierley, I., Rolley, N.J., Jenner, A.J., and Inglis, S.C. (1991). Mutational Analysis of the RNA Pseudoknot Component of a Coronavirus Ribosomal Frameshifting Signal. J. Mol. Biol. *220*, 889–902. https://doi.org/10.1016/0022-2836(91)90361-9.
10. Chamorro, M., Parkin, N., and Varmus, H.E. (1992). An RNA pseudoknot and an optimal heptameric shift site are required for highly efficient ribosomal frameshifting on a retroviral messenger RNA. Proc. Natl. Acad. Sci. USA *89*, 713–717. https://doi.org/10.1073/pnas.89.2.713.
11. Morikawa, S., and Bishop, D.H. (1992). Identification and Analysis of the gag-pal Ribosomal Frameshift Site of Feline Immunodeficiency Virus. Virology *186*, 389–397.
12. Bhatt, P.R., Scaiola, A., Loughran, G., Leibundgut, M., Kratzel, A., Meurs, R., Dreos, R., O'Connor, K.M., McMillan, A., Bode, J.W., et al. (2021). Structural basis of ribosomal frameshifting during translation of the SARS-CoV-2 RNA genome. Science *372*, 1306–1313. https://doi.org/10.1126/science.abf3546.
13. Belcourt, M.F., and Farabaugh, P.J. (1990). Ribosomal frameshifting in the yeast retrotransposon Ty: tRNAs induce slippage on a 7 nucleotide minimal site. Cell *62*, 339–352. https://doi.org/10.1016/0092-8674(90)90371-K.
14. Jacks, T., Madhani, H.D., Masiarz, F.R., and Varmus, H.E. (1988). Signals for Ribosomal Frameshifting in the Rous Sarcoma Virus gag-pol Region. Cell *55*, 447–458. https://doi.org/10.1016/0092-8674(88)90031-1.
15. Brierley, I., Digard, P., and Inglis, S.C. (1989). Characterization of an efficient coronavirus ribosomal frameshifting signal: Requirement for an RNA pseudoknot. Cell *57*, 537–547. https://doi.org/10.1016/0092-8674(89)90124-4.
16. Hou, Y.J., Okuda, K., Edwards, C.E., Martinez, D.R., Asakura, T., Dinnon, K.H., Kato, T., Lee, R.E., Yount, B.L., Mascenik, T.M., et al. (2020). SARS-CoV-2 Reverse Genetics Reveals a Variable Infection Gradient in the Respiratory Tract. Cell *182*, 429–446.e14. https://doi.org/10.1016/j.cell.2020.05.042.
17. Xie, X., Muruato, A., Lokugamage, K.G., Narayanan, K., Zhang, X., Zou, J., Liu, J., Schindewolf, C., Bopp, N.E., Aguilar, P.V., et al. (2020). An Infectious cDNA Clone of SARS-CoV-2. Cell Host Microbe *27*, 841–848.e3. https://doi.org/10.1016/j.chom.2020.04.004.
18. Xie, X., Muruato, A.E., Zhang, X., Lokugamage, K.G., Fontes-Garfias, C.R., Zou, J., Liu, J., Ren, P., Balakrishnan, M., Cihlar, T., et al. (2020). A nanoluciferase SARS-CoV-2 for rapid neutralization testing and screening of anti-infective drugs for COVID-19. Nat. Commun. *11*, 5214. https://doi.org/10.1038/s41467-020-19055-7.
19. Penn, W.D., Harrington, H.R., Schlebach, J.P., and Mukhopadhyay, S. (2020). Regulators of Viral Frameshifting: More Than RNA Influences Translation Events. Annu. Rev. Virol. *7*, 219–238. https://doi.org/10.1146/annurev-virology-012120-101548.
20. Dinman, J.D., and Wickner, R.B. (1992). Ribosomal Frameshifting Efficiency and gag/gag-pol Ratio Are Critical for Yeast M1 Double-Stranded RNA Virus Propagation. J. Virol. *66*, 3669–3676. https://doi.org/10.1128/jvi.66.6.3669-3676.1992.
21. Wu, C.C.C., Peterson, A., Zinshteyn, B., Regot, S., and Green, R. (2020). Ribosome Collisions Trigger General Stress Responses to Regulate Cell Fate. Cell *182*, 404–416.e14. https://doi.org/10.1016/j.cell.2020.06.006.
22. Jousse, C., Oyadomari, S., Novoa, I., Lu, P., Zhang, Y., Harding, H.P., and Ron, D. (2003). Inhibition of a constitutive translation initiation factor 2α phosphatase, CReP, promotes survival of stressed cells. J. Cell Biol. *163*, 767–775. https://doi.org/10.1083/jcb.200308075.
23. Kojima, E., Takeuchi, A., Haneda, M., Yagi, F., Hasegawa, T., Yamaki, K.-I., Takeda, K., Akira, S., Shimokata, K., and Isobe, K.-I. (2003). The function of GADD34 is a recovery from a shutoff of protein synthesis induced by ER stress—elucidation by GADD34-deficient mice. FASEB J. *17*, 1–18. https://doi.org/10.1096/fj.02-1184fje.
24. Marciniak, S.J., Yun, C.Y., Oyadomari, S., Novoa, I., Zhang, Y., Jungreis, R., Nagata, K., Harding, H.P., and Ron, D. (2004). CHOP induces death by promoting protein synthesis and oxidation in the stressed endoplasmic reticulum. Genes Dev. *18*, 3066–3077. https://doi.org/10.1101/gad.1250704.
25. Ma, Y., and Hendershot, L.M. (2003). Delineation of a Negative Feedback Regulatory Loop That Controls Protein Translation during Endoplasmic Reticulum Stress. J. Biol. Chem. *278*, 34864–34873. https://doi.org/10.1074/jbc.M301107200.
26. Zhou, C., Zhang, M., Murray, J., Paulo, J., Gygi, S., Shao, S., Whitman, M., and Keller, T. (2025). GCN1 couples GCN2 to ribosomal state to initiate amino acid response pathway signaling. Science *390*, eads8728. https://doi.org/10.1126/science.ads8728.
27. Darnell, A.M., Subramaniam, A.R., and O'Shea, E.K. (2018). Translational Control through Differential Ribosome Pausing during Amino Acid Limitation in Mammalian Cells. Mol. Cell *71*, 229–243.e11. https://doi.org/10.1016/j.molcel.2018.06.041.

28. Inglis, A.J., Masson, G.R., Shao, S., Perisic, O., McLaughlin, S.H., Hegde, R.S., and Williams, R.L. (2019). Activation of GCN2 by the ribosomal P-stalk. Proc. Natl. Acad. Sci. USA *116*, 4946–4954. https://doi.org/10.1073/pnas.1813352116.

29. Renner, D.M., Parenti, N.A., Bracci, N., and Weiss, S.R. (2025). Betacoronaviruses Differentially Activate the Integrated Stress Response to Optimize Viral Replication in Lung-Derived Cell Lines. Viruses *17*, 120. https://doi.org/10.3390/v17010120.

30. Li, Y., Renner, D.M., Comar, C.E., Whelan, J.N., Reyes, H.M., Cardenas-Diaz, F.L., Truitt, R., Tan, L.H., Dong, B., Alysandratos, K.D., et al. (2021). SARS-CoV-2 induces double-stranded RNA-mediated innate immune responses in respiratory epithelial-derived cells and cardiomyocytes. Proc. Natl. Acad. Sci. USA *118*, e2022643118. https://doi.org/10.1073/pnas.2022643118/-/DCSupplemental.

31. Shaban, M.S., Müller, C., Mayr-Buro, C., Weiser, H., Meier-Soelch, J., Albert, B.V., Weber, A., Linne, U., Hain, T., Babayev, I., et al. (2021). Multi-level inhibition of coronavirus replication by chemical ER stress. Nat. Commun. *12*, 5536. https://doi.org/10.1038/s41467-021-25551-1.

32. Rosa-Fernandes, L., Lazari, L.C., da Silva, J.M., de Morais Gomes, V., Machado, R.R.G., dos Santos, A.F., Araujo, D.B., Coutinho, J.V.P., Arini, G.S., Angeli, C.B., et al. SARS-CoV-2 activates ER stress and Unfolded protein response. Preprint at bioRxiv. https://doi.org/10.1101/2021.06.21.449284.

33. Connor, J.H., and Lyles, D.S. (2002). Vesicular Stomatitis Virus Infection Alters the eIF4F Translation Initiation Complex and Causes Dephosphorylation of the eIF4E Binding Protein 4E-BP1. J. Virol. *76*, 10177–10187. https://doi.org/10.1128/jvi.76.20.10177-10187.2002.

34. Hoang, H.D., Graber, T.E., and Alain, T. (2018). Battling for Ribosomes: Translational Control at the Forefront of the Antiviral Response. J. Mol. Biol. *430*, 1965–1992. https://doi.org/10.1016/j.jmb.2018.04.040.

35. Chuluunbaatar, U., Roller, R., Feldman, M.E., Brown, S., Shokat, K.M., and Mohr, I. (2010). Constitutive mTORC1 activation by a herpesvirus Akt surrogate stimulates mRNA translation and viral replication. Genes Dev. *24*, 2627–2639. https://doi.org/10.1101/gad.1978310.

36. Schubert, K., Karousis, E.D., Jomaa, A., Scaiola, A., Echeverria, B., Gurzeler, L.A., Leibundgut, M., Thiel, V., Mühlemann, O., and Ban, N. (2020). SARS-CoV-2 Nsp1 binds the ribosomal mRNA channel to inhibit translation. Nat. Struct. Mol. Biol. *27*, 959–966. https://doi.org/10.1038/s41594-020-0511-8.

37. Thoms, M., Buschauer, R., Ameismeier, M., Koepke, L., Denk, T., Hirschenberger, M., Kratzat, H., Hayn, M., Mackens-Kiani, T., Cheng, J., et al. (2020). Structural basis for translational shutdown and immune evasion by the Nsp1 protein of SARS-CoV-2. Science *369*, 1249–1255. https://doi.org/10.1126/science.abc8665.

38. Kamitani, W., Huang, C., Narayanan, K., Lokugamage, K.G., and Makino, S. (2009). A two-pronged strategy to suppress host protein synthesis by SARS coronavirus Nsp1 protein. Nat. Struct. Mol. Biol. *16*, 1134–1140. https://doi.org/10.1038/nsmb.1680.

39. Huang, C., Lokugamage, K.G., Rozovics, J.M., Narayanan, K., Semler, B.L., and Makino, S. (2011). SARS coronavirus nsp1 protein induces template-dependent endonucleolytic cleavage of mRNAs: Viral mRNAs are resistant to nsp1-induced RNA cleavage. PLoS Pathog. *7*, e1002433. https://doi.org/10.1371/journal.ppat.1002433.

40. Sinha, N.K., McKenney, C., Yeow, Z.Y., Li, J.J., Nam, K.H., Yaron-Barir, T.M., Johnson, J.L., Huntsman, E.M., Cantley, L.C., Ordureau, A., et al. (2024). The ribotoxic stress response drives UV-mediated cell death. Cell *187*, 3652–3670.e40. https://doi.org/10.1016/j.cell.2024.05.018.

41. Díaz-Bulnes, P., Saiz, M.L., López-Larrea, C., and Rodríguez, R.M. (2020). Crosstalk Between Hypoxia and ER Stress Response: A Key Regulator of Macrophage Polarization. Front. Immunol. *10*, 2951.

42. Baniulyte, G., Durham, S.A., Merchant, L.E., and Sammons, M.A. (2023). Shared Gene Targets of the ATF4 and p53 Transcriptional Networks. Mol. Cell. Biol. *43*, 426–449. https://doi.org/10.1080/10985549.2023.2229225.

43. Tam, A.B., Mercado, E.L., Hoffmann, A., and Niwa, M. (2012). ER Stress Activates NF-κB by Integrating Functions of Basal IKK Activity, IRE1 and PERK. PLoS One *7*, e45078. https://doi.org/10.1371/journal.pone.0045078.

44. Taniuchi, S., Miyake, M., Tsugawa, K., Oyadomari, M., and Oyadomari, S. (2016). Integrated stress response of vertebrates is regulated by four eIF2α kinases. Sci. Rep. *6*, 32886. https://doi.org/10.1038/srep32886.

45. Bertrand, E., Chartrand, P., Schaefer, M., Shenoy, S.M., Singer, R.H., and Long, R.M. (1998). Localization of ASH1 mRNA Particles in Living Yeast. Mol. Cell *2*, 437–445. https://doi.org/10.1016/S1097-2765(00)80143-4.

46. Prasad, V., Cerikan, B., Stahl, Y., Kopp, K., Magg, V., Acosta-Rivero, N., Kim, H., Klein, K., Funaya, C., Haselmann, U., et al. (2023). Enhanced SARS-CoV-2 entry via UPR-dependent AMPK-related kinase NUAK2. Mol. Cell *83*, 2559–2577.e8. https://doi.org/10.1016/j.molcel.2023.06.020.

47. Bonaventura, A., Vecchié, A., Dagna, L., Martinod, K., Dixon, D.L., Van Tassell, B.W., Dentali, F., Montecucco, F., Massberg, S., Levi, M., et al. (2021). Endothelial dysfunction and immunothrombosis as key pathogenic mechanisms in COVID-19. Nat. Rev. Immunol. *21*, 319–329. https://doi.org/10.1038/s41577-021-00536-9.

48. Coley, S.E., Lavi, E., Sawicki, S.G., Fu, L., Schelle, B., Karl, N., Siddell, S.G., and Thiel, V. (2005). Recombinant Mouse Hepatitis Virus Strain A59 from Cloned, Full-Length cDNA Replicates to High Titers In Vitro and Is Fully Pathogenic In Vivo. J. Virol. *79*, 3097–3106. https://doi.org/10.1128/jvi.79.5.3097-3106.2005.

49. Plant, E.P., Rakauskaite, R., Taylor, D.R., and Dinman, J.D. (2010). Achieving a Golden Mean: Mechanisms by Which Coronaviruses Ensure Synthesis of the Correct Stoichiometric Ratios of Viral Proteins. J. Virol. *84*, 4330–4340. https://doi.org/10.1128/jvi.02480-09.

50. Pochopien, A.A., Beckert, B., Kasvandik, S., Berninghausen, O., Beckmann, R., Tenson, T., and Wilson, D.N. (2021). Structure of Gcn1 bound to stalled and colliding 80S ribosomes. Proc. Natl. Acad. Sci. USA *118*, e2022756118. https://doi.org/10.1073/pnas.2022756118/-/DCSupplemental.

51. Wang, X., Mader, M.M., Toth, J.E., Yu, X., Jin, N., Campbell, R.M., Smallwood, J.K., Christe, M.E., Chatterjee, A., Goodson, T., et al. (2005). Complete inhibition of anisomycin and UV radiation but not cytokine induced JNK and p38 activation by an aryl-substituted dihydropyrrolopyrazole quinoline and mixed lineage kinase 7 small interfering RNA. J. Biol. Chem. *280*, 19298–19305. https://doi.org/10.1074/jbc.M413059200.

52. Jandhyala, D.M., Ahluwalia, A., Obrig, T., and Thorpe, C.M. (2008). ZAK: A MAP3Kinase that transduces Shiga toxin- and ricin-induced proinflammatory cytokine expression. Cell. Microbiol. *10*, 1468–1477. https://doi.org/10.1111/j.1462-5822.2008.01139.x.

53. Vind, A.C., Snieckute, G., Blasius, M., Tiedje, C., Krogh, N., Bekker-Jensen, D.B., Andersen, K.L., Nordgaard, C., Tollenaere, M.A.X., Lund, A.H., et al. (2020). ZAKα Recognizes Stalled Ribosomes through Partially Redundant Sensor Domains. Mol. Cell *78*, 700–713.e7. https://doi.org/10.1016/j.molcel.2020.03.021.

54. van Venrooij, W.J., van Eenbergen, J., and Janssen, A.P. (1977). Effect of anisomycin on the cellular level of native ribosomal subunits. Biochemistry *16*, 2343–2348. https://doi.org/10.1021/bi00630a006.

55. Moomau, C., Musalgaonkar, S., Khan, Y.A., Jones, J.E., and Dinman, J.D. (2016). Structural and functional characterization of programmed ribosomal frameshift signals in West Nile virus strains reveals high structural plasticity among cis-acting RNA elements. J. Biol. Chem. *291*, 15788–15795. https://doi.org/10.1074/jbc.M116.735613.

56. Aleksashin, N.A., Langeberg, C.J., Shelke, R.R., Yin, T., and Cate, J.H.D. (2025). RNA elements required for the high efficiency of West Nile virus-induced ribosomal frameshifting. Nucleic Acids Res. *53*, gkae1248. https://doi.org/10.1093/nar/gkae1248.

57. Jiang, G., Santos Rocha, C., Hirao, L.A., Mendes, E.A., Tang, Y., Thompson, G.R., Wong, J.K., and Dandekar, S. (2017). HIV exploits antiviral host innate GCN2-ATF4 signaling for establishing viral replication early in infection. mBio *8*. e01518-16. https://doi.org/10.1128/mBio.01518-16.

58. Aloise, C., Schipper, J.G., van Vliet, A., Oymans, J., Donselaar, T., Hurdiss, D.L., de Groot, R.J., and van Kuppeveld, F.J.M. (2023). SARS-CoV-2 nucleocapsid protein inhibits the PKR-mediated integrated stress response through RNA-binding domain N2b. PLoS Pathog. *19*, e1011582. https://doi.org/10.1371/journal.ppat.1011582.

59. Zheng, Z.Q., Wang, S.Y., Xu, Z.S., Fu, Y.Z., and Wang, Y.Y. (2021). SARS-CoV-2 nucleocapsid protein impairs stress granule formation to promote viral replication. Cell Discov. *7*, 38. https://doi.org/10.1038/s41421-021-00275-0.

60. Gibbs, V.J., Lin, Y.H., Ghuge, A.A., Anderson, R.A., Schiemann, A.H., Conaglen, L., Sansom, B.J.M., da Silva, R.C., and Sattlegger, E. (2024). GCN2 in Viral Defence and the Subversive Tactics Employed by Viruses. J. Mol. Biol. *436*, 168594. https://doi.org/10.1016/j.jmb.2024.168594.

61. Ventoso, I., Sanz, M.A., Molina, S., Berlanga, J.J., Carrasco, L., and Esteban, M. (2006). Translational resistance of late alphavirus mRNA to eIF2α phosphorylation: A strategy to overcome the antiviral effect of protein kinase PKR. Genes Dev. *20*, 87–100. https://doi.org/10.1101/gad.357006.

62. Caselli, E., Benedetti, S., Gentili, V., Grigolato, J., and Di Luca, D. (2012). Short Communication: Activating Transcription Factor 4 (ATF4) Promotes HIV Type 1 Activation. AIDS Res. Hum. Retrovir. *28*, 907–912. https://doi.org/10.1089/aid.2011.0252.

63. Schoof, M., Wang, L., Cogan, J.Z., Lawrence, R.E., Boone, M., Wuerth, J.D., Frost, A., and Walter, P. (2021). Viral evasion of the integrated stress response through antagonism of eIF2-P binding to eIF2B. Nat. Commun. *12*, 7103. https://doi.org/10.1038/s41467-021-26164-4.

64. De Miguel, C., Thorkelsson, S.R., Fatalska, A., Hodgson, G., Wang, C., and Bertolotti, A. (2026). Termination of the integrated stress response. Science *391*, eadw5137. https://doi.org/10.1126/science.adw5137.

65. Aviner, R., Lidsky, P.V., Xiao, Y., Tassetto, M., Kim, D., Zhang, L., McAlpine, P.L., Elias, J., Frydman, J., and Andino, R. (2024). SARS-CoV-2 Nsp1 cooperates with initiation factors EIF1 and 1A to selectively enhance translation of viral RNA. PLoS Pathog. *20*, e1011535. https://doi.org/10.1371/journal.ppat.1011535.

66. Melian, E.B., Hinzman, E., Nagasaki, T., Firth, A.E., Wills, N.M., Nouwens, A.S., Blitvich, B.J., Leung, J., Funk, A., Atkins, J.F., et al. (2010). NS1′ of Flaviviruses in the Japanese Encephalitis Virus Serogroup Is a Product of Ribosomal Frameshifting and Plays a Role in Viral Neuroinvasiveness. J. Virol. *84*, 1641–1647. https://doi.org/10.1128/jvi.01979-09.

67. Medigeshi, G.R., Lancaster, A.M., Hirsch, A.J., Briese, T., Lipkin, W.I., Defilippis, V., Früh, K., Mason, P.W., Nikolich-Zugich, J., and Nelson, J.A. (2007). West Nile Virus Infection Activates the Unfolded Protein Response, Leading to CHOP Induction and Apoptosis. J. Virol. *81*, 10849–10860. https://doi.org/10.1128/jvi.01151-07.

68. Roth, H., Magg, V., Uch, F., Mutz, P., Klein, P., Haneke, K., Lohmann, V., Bartenschlager, R., Fackler, O.T., Locker, N., et al. (2017). Flavivirus Infection Uncouples Translation Suppression from Cellular Stress Responses. mBio *8*. e02150-16. https://doi.org/10.1128/mbio.02150-16.

69. Oltion, K., Carelli, J.D., Yang, T., See, S.K., Wang, H.Y., Kampmann, M., and Taunton, J. (2023). An E3 ligase network engages GCN1 to promote the degradation of translation factors on stalled ribosomes. Cell *186*, 346–362.e17. https://doi.org/10.1016/j.cell.2022.12.025.

70. Müller, M.B.D., Kasturi, P., Jayaraj, G.G., and Hartl, F.U. (2023). Mechanisms of readthrough mitigation reveal principles of GCN1-mediated translational quality control. Cell *186*, 3227–3244.e20. https://doi.org/10.1016/j.cell.2023.05.035.

71. Robinson, K.S., Toh, G.A., Firdaus, M.J., Tham, K.C., Rozario, P., Lim, C.K., Toh, Y.X., Lau, Z.H., Binder, S.C., Mayer, J., et al. (2023). Diphtheria toxin activates ribotoxic stress and NLRP1 inflammasome-driven pyroptosis. J. Exp. Med. *220*, e20230105. https://doi.org/10.1084/jem.20230105.

72. Subramanian, A., Wang, L., Moss, T., Voorhies, M., Sangwan, S., Stevenson, E., Pulido, E.H., Kwok, S., Chalkley, R.J., Li, K.H., et al. (2023). A Legionella toxin exhibits tRNA mimicry and glycosyl transferase activity to target the translation machinery and trigger a ribotoxic stress response. Nat. Cell Biol. *25*, 1600–1615. https://doi.org/10.1038/s41556-023-01248-z.

73. Finkel, Y., Mizrahi, O., Nachshon, A., Weingarten-Gabbay, S., Morgenstern, D., Yahalom-Ronen, Y., Tamir, H., Achdout, H., Stein, D., Israeli, O., et al. (2021). The coding capacity of SARS-CoV-2. Nature *589*, 125–130. https://doi.org/10.1038/s41586-020-2739-1.

74. Puray-Chavez, M., Lee, N., Tenneti, K., Wang, Y., Vuong, H.R., Liu, Y., Horani, A., Huang, T., Gunsten, S.P., Case, J.B., et al. (2022). The Translational Landscape of SARS-CoV-2-infected Cells Reveals Suppression of Innate Immune Genes. mBio *13*, e0081522. https://doi.org/10.1128/mbio.00815-22.

75. Kim, D., Kim, S., Park, J., Chang, H.R., Chang, J., Ahn, J., Park, H., Park, J., Son, N., Kang, G., et al. (2021). A high-resolution temporal atlas of the SARS-CoV-2 translatome and transcriptome. Nat. Commun. *12*, 5120. https://doi.org/10.1038/s41467-021-25361-5.

76. Irigoyen, N., Firth, A.E., Jones, J.D., Chung, B.Y.-W., Siddell, S.G., and Brierley, I. (2016). High-Resolution Analysis of Coronavirus Gene Expression by RNA Sequencing and Ribosome Profiling. PLoS Pathog. *12*, e1005473. https://doi.org/10.1371/journal.ppat.1005473.

77. Zeng, F., Li, X., Pires-Alves, M., Chen, X., Hawk, C.W., and Jin, H. (2021). Conserved heterodimeric GTPase Rbg1/Tma46 promotes efficient translation in eukaryotic cells. Cell Rep. *37*, 109877. https://doi.org/10.1016/j.celrep.2021.109877.

78. Meydan, S., and Guydosh, N.R. (2020). Disome and Trisome Profiling Reveal Genome-wide Targets of Ribosome Quality Control. Mol. Cell *79*, 588–602.e6. https://doi.org/10.1016/j.molcel.2020.06.010.

79. Yan, L.L., and Zaher, H.S. (2021). Ribosome quality control antagonizes the activation of the integrated stress response on colliding ribosomes. Mol. Cell *81*, 614–628.e4. https://doi.org/10.1016/j.molcel.2020.11.033.

80. Joazeiro, C.A.P. (2019). Mechanisms and functions of ribosome-associated protein quality control. Nat. Rev. Mol. Cell Biol. *20*, 368–383. https://doi.org/10.1038/s41580-019-0118-2.

81. Huang, H., Weng, H., Sun, W., Qin, X., Shi, H., Wu, H., Zhao, B.S., Mesquita, A., Liu, C., Yuan, C.L., et al. (2018). Recognition of RNA N6-methyladenosine by IGF2BP proteins enhances mRNA stability and translation. Nat. Cell Biol. *20*, 285–295. https://doi.org/10.1038/s41556-018-0045-z.

82. Mao, Y., Dong, L., Liu, X.M., Guo, J., Ma, H., Shen, B., and Qian, S.B. (2019). m6A in mRNA coding regions promotes translation via the RNA helicase-containing YTHDC2. Nat. Commun. *10*, 5332. https://doi.org/10.1038/s41467-019-13317-9.

83. Murakami, S., Olarerin-George, A.O., Liu, J.F., Zaccara, S., Hawley, B., and Jaffrey, S.R. (2025). m^6A alters ribosome dynamics to initiate mRNA degradation. Cell *188*, 3728–3743.e20. https://doi.org/10.1016/j.cell.2025.04.020.

84. Adachi, A., Gendelman, H.E., Koenig, S., Folks, T., Willey, R., Rabson, A., and Martin, M.A. (1986). Production of acquired immunodeficiency syndrome-associated retrovirus in human and nonhuman cells transfected with an infectious molecular clone. J. Virol. *59*, 284–291. https://doi.org/10.1128/jvi.59.2.284-291.1986.

85. Bojkova, D., Klann, K., Koch, B., Widera, M., Krause, D., Ciesek, S., Cinatl, J., and Münch, C. (2020). Proteomics of SARS-CoV-2-infected host cells reveals therapy targets. Nature *583*, 469–472. https://doi.org/10.1038/s41586-020-2332-7.

86. Widera, M., Wilhelm, A., Toptan, T., Raffel, J.M., Kowarz, E., Roesmann, F., Grözinger, F., Siemund, A.L., Luciano, V., Külp, M., et al. (2021). Generation of a Sleeping Beauty Transposon-Based Cellular System for Rapid and Sensitive Screening for Compounds and Cellular Factors Limiting SARS-CoV-2 Replication. Front. Microbiol. *12*, 701198. https://doi.org/10.3389/fmicb.2021.701198.

87. Fusco, D., Accornero, N., Lavoie, B., Shenoy, S.M., Blanchard, J.-M., Singer, R.H., Bertrand, E., and Biol, C. (2003). Single mRNA Molecules Demonstrate Probabilistic Movement in Living Mammalian Cells. Curr. Biol. *13*, 161–167.

88. Mendez, A.S., Ly, M., González-Sánchez, A.M., Hartenian, E., Ingolia, N.T., Cate, J.H., and Glaunsinger, B.A. (2021). The N-terminal domain of SARS-CoV-2 nsp1 plays key roles in suppression of cellular gene expression and preservation of viral gene expression. Cell Rep. *37*, 109841. https://doi.org/10.1016/j.celrep.2021.109841.

89. da Veiga Leprevost, F., Haynes, S.E., Avtonomov, D.M., Chang, H.-Y., Shanmugam, A.K., Mellacheruvu, D., Kong, A.T., and Nesvizhskii, A.I. (2020). Philosopher: a versatile toolkit for shotgun proteomics data analysis. Nat. Methods *17*, 869–870. https://doi.org/10.1038/s41592-020-0912-y.

90. Yu, F., Haynes, S.E., and Nesvizhskii, A.I. (2021). IonQuant Enables Accurate and Sensitive Label-Free Quantification With FDR-Controlled Match-Between-Runs. Mol. Cell. Proteomics *20*, 100077. https://doi.org/10.1016/j.mcpro.2021.100077.

91. Hsiao, Y., Zhang, H., Li, G.X., Deng, Y., Yu, F., Valipour Kahrood, H., Steele, J.R., Schittenhelm, R.B., and Nesvizhskii, A.I. (2024). Analysis and Visualization of Quantitative Proteomics Data Using FragPipe-Analyst. J. Proteome Res. *23*, 4303–4315. https://doi.org/10.1021/acs.jproteome.4c00294.

92. Kong, A.T., Leprevost, F.V., Avtonomov, D.M., Mellacheruvu, D., and Nesvizhskii, A.I. (2017). MSFragger: Ultrafast and comprehensive peptide identification in mass spectrometry-based proteomics. Nat. Methods *14*, 513–520. https://doi.org/10.1038/nmeth.4256.

93. van Wetering, S., van der Linden, A.C., van Sterkenburg, M.A., de Boer, W.I., Kuijpers, A.L., Schalkwijk, J., and Hiemstra, P.S. (2000). Regulation of SLPI and elafin release from bronchial epithelial cells by neutrophil defensins. Am. J. Physiol., Lung Cell. Mol. Physiol. *278*, L51–L58. https://doi.org/10.1152/ajplung.2000.278.1.l51.

94. Grentzmann, G., Ingram, J.A., Kelly, P.J., Gesteland, R.F., and Atkins, J.F. (1998). A dual-luciferase reporter system for studying recoding signals. RNA *4*, 479–486.

95. Prieto-Garcia, C., Hartmann, O., Reissland, M., Braun, F., Fischer, T., Walz, S., Schülein-Völk, C., Eilers, U., Ade, C.P., Calzado, M.A., et al. (2020). Maintaining protein stability of ΔNp63 via USP28 is required by squamous cancer cells. EMBO Mol. Med. *12*, e11101. https://doi.org/10.15252/emmm.201911101.

96. Toptan, T., Hoehl, S., Westhaus, S., Bojkova, D., Berger, A., Rotter, B., Hoffmeier, K., Cinatl, J., Ciesek, S., and Widera, M. (2020). Optimized qRT-PCR approach for the detection of intra- and extra-cellular SARS-CoV-2 RNAs. Int. J. Mol. Sci. *21*, 4396. https://doi.org/10.3390/ijms21124396.

97. Wilhelm, A., Toptan, T., Pallas, C., Wolf, T., Goetsch, U., Gottschalk, R., Vehreschild, M.J.G.T., Ciesek, S., and Widera, M. (2021). Antibody-mediated neutralization of authentic sars-cov-2 B.1.617 Variants Harboring L452R and T478K/E484Q. Viruses *13*, 1693. https://doi.org/10.3390/v13091693.

98. Wilhelm, A., Widera, M., Grikscheit, K., Toptan, T., Schenk, B., Pallas, C., Metzler, M., Kohmer, N., Hoehl, S., Marschalek, R., et al. (2022). Limited neutralisation of the SARS-CoV-2 Omicron subvariants BA.1 and BA.2 by convalescent and vaccine serum and monoclonal antibodies. EBioMedicine *82*, 104158. https://doi.org/10.1016/j.ebiom.2022.104158.

99. Xiao, S.Y., Guzman, H., Zhang, H., Travassos da Rosa, A.P., and Tesh, R.B. (2001). West Nile virus infection in the golden hamster (Mesocricetus auratus): a model for West Nile encephalitis. Emerg. Infect. Dis. *7*, 714–721. https://doi.org/10.3201/eid0704.010420.

100. Sertznig, H., Roesmann, F., Wilhelm, A., Heininger, D., Bleekmann, B., Elsner, C., Santiago, M., Schuhenn, J., Karakoese, Z., Benatzy, Y., et al. (2022). SRSF1 acts as an IFN-I-regulated cellular dependency factor decisively affecting HIV-1 post-integration steps. Front. Immunol. *13*, 935800. https://doi.org/10.3389/fimmu.2022.935800.

101. Roesmann, F., Sertznig, H., Klaassen, K., Wilhelm, A., Heininger, D., Heß, S., Elsner, C., Marschalek, R., Santiago, M.L., Esser, S., et al. (2024). The interferon-regulated host factor hnRNPA0 modulates HIV-1 production by interference with LTR activity, mRNA trafficking, and programmed ribosomal frameshifting. J. Virol. *98*, e0053424. https://doi.org/10.1128/jvi.00534-24.

102. Widera, M., Westhaus, S., Rabenau, H.F., Hoehl, S., Bojkova, D., Cinatl, J., and Ciesek, S. (2021). Evaluation of stability and inactivation methods of SARS-CoV-2 in context of laboratory settings. Med. Microbiol. Immunol. *210*, 235–244. https://doi.org/10.1007/s00430-021-00716-3.

103. Freed, N.E., Vlková, M., Faisal, M.B., and Silander, O.K. (2020). Rapid and inexpensive whole-genome sequencing of SARS-CoV-2 using 1200 bp tiled amplicons and Oxford nanopore Rapid Barcoding. Biol. Methods Protoc. *5*, bpaa014. https://doi.org/10.1093/biomethods/bpaa014.

104. EPI2ME Labs. (2024). ARTIC SARS-CoV-2 Workflow. GitHub. https://github.com/epi2me-labs/wf-artic.

105. Shu, Y., and McCauley, J. (2017). GISAID: Global initiative on sharing all influenza data – from vision to reality. Euro Surveill. *22*, 30494. https://doi.org/10.2807/1560-7917.ES.2017.22.13.30494.

106. Aksamentov, I., Roemer, C., Hodcroft, E., and Neher, R. (2021). Nextclade: clade assignment, mutation calling and quality control for viral genomes. J. Open Source Softw. *6*, 3773. https://doi.org/10.21105/joss.03773.

Please cite this article in press as: Xavier et al., Programmed ribosomal frameshifting triggers translational stress to promote viral replication, Cell (2026), https://doi.org/10.1016/j.cell.2026.08.031

CellPress
OPEN ACCESS

STAR★METHODS

KEY RESOURCES TABLE

REAGENT or RESOURCE	SOURCE	IDENTIFIER
Antibodies		
Anti β-actin (mouse)	Santa cruz	sc-47778, RRID: AB_626632
Anti GCN2 (rabbit)	Cell signaling technology	40457, RRID: AB_2277617
Anti-GCN2 (phospho T899) antibody (rabbit)	abcam	ab75836, RRID: AB_1310260
Anti PKR (rabbit)	Cell signaling technology	3072, RRID: AB_2277600
Anti p-PKR (rabbit)	Cell signaling technology	3076
Anti PERK (rabbit)	Cell signaling technology	5683, RRID: AB_10841299
Anti HRI (mouse)	Santa cruz	sc-365239, RRID: AB_10843794
Anti eIF2α (rabbit)	Cell signaling technology	9722, RRID: AB_2230924
Anti p-eIF2α S51 (rabbit)	Cell signaling technology	9721, RRID: AB_330951
Anti ATF4 (rabbit)	Cell signaling technology	11815, RRID: AB_2616025
Anti ATF6 (mouse)	Novus biological	NBP1-40256SS; RRID:AB_2058775
Anti Zakα (rabbit)	Bethyl laboratories	A301-993A, RRID: AB_1576612
Anti HIV-1 p15 (rabbit)	abcam	ab66951, RRID: AB_1139523
Goat anti-mouse HRP	Santa cruz	sc-2031, RRID: AB_631737
Goat anti rabbit HRP	Dako/Agilent	P0448, RRID: AB_2617138
Anti puromycin(mouse)	Sigma-Aldrich	MABE343, RRID: AB_2566826
Anti-Phospho-SAPK/JNK (Thr183/Tyr185)	Cell signaling technology	#9251, RRID: AB_331659
Anti-SAPK/JNK	Cell signaling technology	#9252, RRID: AB_2250373
Anti-p38 MAPK	Cell signaling technology	#9212, RRID: AB_330713
Anti-phospho-p38 MAPK	Cell signaling technology	#4511, RRID: AB_2139682
Anti-phospho-Zakα	invitrogen	# PA5-105924; RRID:AB_2817323
Bacterial and virus strains		
SARS-CoV-2 variant B.1	N/A	FFM7/2020; MT358643
SARS-CoV-2 variant Delta B.1.617.2	N/A	FFM-IND8424/2020; MZ31514
SARS-CoV-2 Omicron BA.1/B.1.1.529a	N/A	2021; EPI_ISL_6959868
SARS-CoV-2 JN-1	N/A	EPI_ISL_19621541
HIV-1 NL4-3	Adachi et al.[84]	GenBank: M19921
West Nile Virus NY-99	This study	N/A
Chemicals, peptides, and recombinant proteins		
Anisomycin	MERCK	A9789-25MG
Doxycyclin-Hyclat	MERCK	D5207-1G
Dimethylsulfoxide (DMSO)	Carl ROTH	7029.1
Critical commercial assays		
Dual-Glo® Luciferase Assay System	Promega	E2920
Deposited data		
RNA-seq	This study	GEO: GSE322665
Proteomics	This study	PRIDE: PXD057424
Experimental models: Cell lines		
Huh7	JCRB	RRID:CVCL_0336
HEK293T	ATCC	CRL-3216, RRID:CVCL_0063
A549 ACE2+TMPRSS2	Widera et al.[86]	N/A
ARPE-19	ATCC	RRID:CVCL_0145

(*Continued on next page*)

Please cite this article in press as: Xavier et al., Programmed ribosomal frameshifting triggers translational stress to promote viral replication, Cell (2026), https://doi.org/10.1016/j.cell.2026.08.031

Continued

REAGENT or RESOURCE	SOURCE	IDENTIFIER
Caco2	Bojkova et al.[85] and Widera et al.[86]	RRID: CVCL_0025
Calu3	ATCC	HTB-55, RRID:CVCL_0609
Oligonucleotides		
GATCAACTCCGCGAACCCAT (disome fw)	This study	N/A
GCATTACACCGCAAACCCTT (disome rv)	This study	N/A
GGTTTGCGGTGTAAGTGCAG (FS fw)	This study	N/A
AGACGAGGTCTGCCATTGTG (FS rv)	This study	N/A
GGTTTGCGGTGTAAGAGCC (ΔL1 fw)	This study	N/A
AGACGAGGTCTGCCATTGTG (ΔL1 rv)	This study	N/A
5'-GTAGTAACAAACCCACGTATA-3' (sictrl)	Sigma-Aldrich	N/A
5'-GCCUAACUGGUGAAGAAGUAU-3' (siGCN2)	Sigma-Aldrich	N/A
5'-GGAACGACCUGAAGCUAUAAA-3' (siPERK)	Sigma-Aldrich	N/A
5'-ACGAGAGAUUAACCAUUCCAA-3'(siZakα)	Sigma-Aldrich	N/A
5'-GCUGAACUUCUUCAUGUAUGU-3' (siPKR)	Sigma-Aldrich	N/A
5'-AGCUACUUUGCCAGACGUUUA-3'(siHRI)	Sigma-Aldrich	N/A
siRNA screen (Figure 5B)	Dharmacon	See Table S2
Recombinant DNA		
P2Luc SARS-CoV-2 FS	This study	N/A
P2Luc SARS-CoV-2 ΔL1	This study	N/A
P2luc SARS-CoV-2 IFC	This study	N/A
pcDNA 3.1 2luc SARS-CoV-2 FS	This study	N/A
pcDNA 3.1 2luc SARS-CoV-2 ΔL1	This study	N/A
pcDNA 3.1 2luc SARS-CoV-2 IFC	This study	N/A
pcDNA 3.1 2luc SARS-CoV-2 SSM	This study	N/A
pcDNA 3.1 2luc SARS-CoV-2 PreM	This study	N/A
pcDNA 3.1 2luc SARS-CoV-2 PS	This study	N/A
pcDNA 3.1 2luc HIV-1-1 FS	This study	N/A
pcDNA 3.1 2luc HIV-1-1 ctrl	This study	N/A
pcDNA 3.1 2luc HIV-1-1 ΔSL	This study	N/A
pcDNA 3.1 2luc HIV-1-1 SSM	This study	N/A
pcDNA 3.1 2luc WNV FS	This study	N/A
pcDNA 3.1 2luc WNV ctrl	This study	N/A
pcDNA 3.1 2luc WNV ΔPK	This study	N/A
pcDNA 3.1 2luc WNV SSM	This study	N/A
pcDNA 3.1 MS2L FS	This study	N/A
pcDNA 3.1 MS2L ΔL1	This study	N/A
pCMV myc GCN2 HRS	This study	N/A
pCMV myc GCN2 KD	This study	N/A
pLVX dox ATF4	This study	N/A
pMS2-GFP	Fusco et al.[87]	Addgene #27121
pNL4-3	Adachi et al.[84]	GenBank: M19921
Flag Nsp1	Mendez et al.[88]	Addgene #176057
Software and algorithms		
BioRender	N/A	Biorender.com
Philosopher v.5.1.0	da Veiga Leprevost[89]	https://github.com/Nesvilab/philosopher/releases
IonQuant v.1.10.27	Yu et al.[90]	https://github.com/Nesvilab/IonQuant
FragPipe Analyst	Hsiao et al.[91]	http://fragpipe-analyst.nesvilab.org/
FragPipe v21.1 with MSFragger v.4.0	Kong et al.[92]	https://fragpipe.nesvilab.org/

Please cite this article in press as: Xavier et al., Programmed ribosomal frameshifting triggers translational stress to promote viral replication, Cell (2026), https://doi.org/10.1016/j.cell.2026.08.031

EXPERIMENTAL MODEL AND STUDY PARTICIPANT DETAILS

Cell culture

Calu-3 lung epithelial cells were cultured in Dulbecco's modified Eagle's Medium (DMEM)-F12 (Gibco) with 10 % fetal calf serum (FCS), 100 IU/ml of Penicillin and 100 μg/ml of Streptomycin and A549 ACE2+TMPRSS2 (A549 A+T)[86] and ARPE-19 cells were grown in Minimal Essential Medium (MEM) supplemented with 10 % fetal calf serum (FCS), 4 mM L-glutamine, 100 IU/ml of Penicillin, 100 μg/ml of Streptomycin at 37°C and 5 % carbon dioxide. HEK293T cells were cultured with DMEM (Gibco) supplemented with 10% FCS and 100 IU/ml of Penicillin and 100 μg/ml of Streptomycin. Jurkat cells were cultured with RPMI (Gibco) supplemented with 10% FCS and 100 IU/ml of Penicillin and 100 μg/ml of Streptomycin. Lung tissue of emphysema patients was used for the isolation of primary human broncial epithelial (HBE) cells as described elsewhere[93] with written informed consent from all patients. Keratinocyte-SFM medium (Gibco) supplemented with bovine pituitary extract (25 μg/ml, Gibco), human recombinant epidermal growth factor (0.2 ng/ml, Gibco), isoproterenol (1 nM, Sigma), antibiotic/antimycotic solution (Sigma-Aldrich) and MycoZap Plus PR (Lonza) was used for the expansion of basal cells which were subsequently cryopreserved until further use. In PneumaCult-Ex medium (StemCell Technologies), cells were passaged once and seeded on 12-well transwell inserts (Sarstedt) at 4 x 10^4 cells/insert for differentiation. Once the cell layers were confluent, apical medium was removed and basal medium exchanged to PneumaCult ALI Maintenance Medium (StemCell Technologies) supplemented with antibiotic/antimycotic solution (Sigma-Aldrich) and MycoZap Plus PR (Lonza). The cell layers were washed with PBS and basal medium changed every day for a period of four weeks. Differentiation was successful by the appearance of ciliated cells with ciliary movement, mucus production and an increase of transepithelial electric resistance (TEER) which indicates tight junction formation. TZM-bl cells were cultured at 37 °C and 5% CO_2 using DMEM supplemented with 10% (v/v) heat-inactivated fetal calf serum (FCS), 50 μg/ml of penicillin and streptomycin (P/S) each (Invitrogen). Jurkat cells were maintained in RPMI 1640 medium (Invitrogen) supplemented with 10% FCS and P/S (50 μg/ml each, Invitrogen) at 37 °C and 5% CO_2.

METHOD DETAILS

Western blotting

Harvested cells were lysed in lysis buffer (50mM Tris-HCl pH 7.5, 150mM NaCl, 1% NP-40) freshly supplemented with protease inhibitor cocktail (Roche) and phosphatase inhibitor cocktail (Sigma) for 20 minutes on ice. Lysates were cleared by centrifuging in 16,000 g for 20 min at 4 °C. Protein concentration was measured by BCA method (Thermofisher), and lysates were boiled in Laemmli buffer with beta-mercaptoethanol for 10 min. After treatment and infection, confluent 12-well plates of Calu-3 cells were lysed with 200 μl Triton-X lysis buffer supplemented with Protease- and Phosphataseinhibitors (Merck, cOmplete™ Protease inhibitor-Cocktail #11697498001 PhosSTOP™ #04906837001). An equal volume of Laemmli buffer (Sigma) supplemented with 5 % ß-mercaptoethanol was added and samples were stored at -20 °C until further analysis. Denatured lysates were separated by SDS-PAGE, transferred into PVDF membrane, blocked with 5% milk and 0.1% Tween-20 in PBS, and incubated overnight in 4 °C with primary antibodies diluted in 5% BSA and 0.1% Tween-20 in PBS. After washing three times with PBST, membranes were incubated with secondary antibodies diluted in blocking solution for one hour at room temperature. After PBST washing, membranes were developed with prime ECL (Amarsham) for regular Western blotting experiments or with SuperSignal ECL (Thermo Fisher) for FACS sorted samples and imaged using Chemi-Capt 5000 software.

Cell culture and plasmid/siRNA transfection

HEK293T, Huh7, A549, Caco2 and Calu-3 were obtained from ATCC. For maintaining each cell line, the following media were used: HEK293T (4.5g/L DMEM, 10% FCS and Penicillin/Streptomycin), Huh7 (4.5g/L DMEM, 10% FCS, 1mM Sodium Pyruvate, NEAA (non-essential amino acids) and gentamicin), A549 (1g/L DMEM, 10% FCS and gentamicin), Caco2 (MEM, 20% FCS, 1mM Sodium Pyruvate, NEAA and gentamicin). For plasmid transfection, we used Fugene HD reagent (Promega) according to manufacturer's guideline. Per 6cm culture dish, we used 4 μg of plasmids and 12 μl of Fugene HD. Cells were typically harvested 48 hours after transfection. siRNAs were synthesized by Sigma Aldrich with dTdT overhangs and dissolved at 20 μM in ultra-pure water. siRNA transfection was performed using Lipofectamine RNAiMax reagent (Thermofisher) according to manufacturer's guideline. When siRNA and plasmid transfections were combined, siRNA transfections were performed first, and plasmids were transfected 24 hours later, except pNL4-3 and siRNA transfection, which occurred simultaneously.

Frameshift assay by luminescence

Harvested cells were proceeded according to manufacturer's guideline of Dual-Luciferase Reporter Assay System (Promega). Luminescence signal was measured using Pherastar FSX microplate reader from BMG Labtech. Frameshifting efficiencies (% frameshifting) were determined by calculating relative luciferase activities (firefly/Renilla) from test constructs and dividing by relative luciferase activities from replicate wells of matched in-frame control constructs. Frameshifting efficiency of FS construct was set to 100%.

FACS sorting of cells with or without frameshift

For this, we used pcDNA3.1-mCherry-SARS-CoV-2 pseudoknot (or ΔL1 control)-GFP reporter plasmid. Transfected cells were detached by trypsinization and resuspended in PBS + 1% FCS. Cells were further passed through 0.22μm filter tube (Falcon 11821070)

Please cite this article in press as: Xavier et al., Programmed ribosomal frameshifting triggers translational stress to promote viral replication, Cell (2026), https://doi.org/10.1016/j.cell.2026.08.031

before loading on the FACS. Sorting was performed using sony cell sorter SH800S. After gating on FCS/SSC, doublets were removed by gating against SSC-H/SSC-W and FSC-H/FSC-W. GFP and mCherry signals were measured on singlets. For control and pseudoknot plasmids, we sorted 10,000-20,000 mCherry and GFP positive cells, respectively. For siControl and siGcn2, GFP positive cells were sorted. Non-transfected cells were included each time to obtain a confident threshold for mCherry or GFP positive cells. Throughout all procedures after trypsinization, the samples were kept on 4 °C. Immediately after sorting, cells were pelleted by centrifuging 14,000 g for 2 min at 4 °C and lysed with ice cold RIPA buffer.

Plasmid construction

Pseudoknot sequence of SARS-CoV-2 was synthesized in pBluescript KS plasmid by Genscript as below. ΔL1 control sequence was constructed by deleting the nucleotides indicated in bold. Pseudoknot and ΔL1 sequences were then amplified by PCR and subcloned between Renilla and Luciferase genes in p2Luc plasmid[94] (GenBank: OX368027.1 nt 13016-13989).To enable more flexible sub-cloning, we also sub-cloned the entire renilla-firefly-luciferase cassette into pcDNA3.1 with modified restriction sites (BamH1 and EcoR1) between renilla and firefly luciferase(pcDNA 3.1 2luc)). Using this as template, we cloned the MS2 constructs (Figures S2A and S2B) without renilla and firefly and constructs with different STOP codon positions, as well as WNV and HIV-1-1 constructs (Figure 4A). For HIV-1-1 FS we cloned HIV-1-1 isolate 1994-12 nucleotides 1248 to 1350 (Genbank ID: FJ155104.1) into pcDNA 3.1 2Luc using BamHI/EcoRI restriction sites. For HIV-1 SSM we replaced the slippery site (TTTTTTA)with a mutant slippery site (CTTCCTCA). For HIV-1 IFC we replaced the slippery site with the mutant slippery site from SSM and added an additional adenosine base at the end of the slippery site to have renilla and firefly luciferases in the same frame. HIV-1 ΔSL construct harbors a deletion of the entire stem loop sequence (AGGGAAGATCTGGCCTTCCTACAAGGGAAGGCCAGGGAATTTTCTTCAG). WNV FS, IFC and SSM were cloned into pcDNA 3.1 2Luc using BamHI/EcoRI restriction sites based on sequences from Aleksashin et al.[56]

RNA-transfection

Template DNA for mRNA SARS-CoV-2 deltaL1 and FS was linearized and used for in vitro transcription using the mMESSAGE mMACHINE™ T7 Ultra Kit (Thermo Fisher Scientific), which incorporates a 5′-cap analog and a 3′-poly(A) tail during transcription. The quality and integrity of synthesized mRNAs were confirmed by agarose gel electrophoresis and nano drop measurement. Equimolar amounts of mRNAs were transfected into cells using Lipofectamine™ MessengerMAX™ Transfection Reagent (Thermo Fisher Scientific), following the manufacturer's protocol. For a 60-mm dish, 2 μg of each mRNA was transfected in Opti-MEM™ reduced serum medium (Thermo Fisher Scientific), and cells were harvested at the indicated time points for downstream analysis.

RNA-Sequencing

Total RNA was extracted from HEK293T cells using the RNeasy Plus Kit (Qiagen) according to the manufacturer's instructions. NGS library prep was performed with Illumina's Stranded mRNA Prep Ligation Kit following Stranded mRNA Prep Ligation ReferenceGuide (October 2023) (Document 1000000124518 v04). Libraries were prepared with a starting amount of 1000 ng and amplified in 8 PCR cycles. Two post PCR purification steps were performed to exclude residual primer and adapter dimers. Libraries were profiled in a High Sensitivity DNA chip on a 2100 Bioanalyzer (Agilent technologies) and quantified using the Qubit 1x dsDNA HS Assay Kit, in a Qubit 4.0 Fluorometer (Invitrogen by Thermo Fisher Scientific). All 12 samples were pooled in equimolar ratio and sequenced on 1 NextSeq 2000 P2 (100 cycles) FC, SR for 116 cycles plus 2x10 cycles for the dual index read and 1 dark cycle upfront R1. Raw reads were quality-assessed with FastQC (v.0.11.9) and aligned to the human genome (GRCh38.p14 assembly) with gene annotation from Gencode release 48 using STAR (v.2.7.10a) with parameter „–outFilterMismatchNoverLmax 0.04". Secondary alignments were removed with Samtools (v.1.10). Mapped data quality was assessed using QualiMap (v.2.2.1) and dupRadar (v.1.37.0). Read counts were summarized on the gene level with Subread featureCounts (v.2.0.0) using stranded parameter "-s 2" and the above-mentioned annotation file. Differential expression analysis was performed using DESeq2 (v.1.42.0) following the standard data processing workflow with the default median-ratio normalisation, dispersion estimation, negative binomial GLM fitting and Wald statistics for pairwise comparisons with independent gene filtering and 5% FDR threshold. DESeq2-normalised FPM (fragments per million) and FPKM (fragments per kilobase per million) expression values per gene were calculated in all samples and the latter were used for plotting expression heatmaps of DEGs in R (v.4.5.1) with libraries pheatmap and RcolorBrewer using Z-score normalisation and hierarchical clustering of genes based on Pearson's correlation with average linkage. Principal component analysis (PCA) based on the 500 most variable genes and sample-to-sample clustering based on Euclidean distance were performed on rlog-transformed counts and plotted following the standard DESeq2 analytical workflow. Drug mimetic enrichment analysis using the up-regulated DEGs from the FS versus ΔL1 differential comparison against the Novartis DRUG-seq U2OS MoABox open-source dataset was perfromed with DRUG-seqr and a bubble plot of selected top hits (translation inhibitor drugs) was produced using the ggplot2 library in R (v.4.5.1). Bubble plots of significantly enriched "hallmark signatures" from the Molecular Signature Database (MsigDB) were prepared with ShinyGO (v0.85.1) using the up- or down-regulated DEGs from the FS versus ΔL1 differential comparison and a background set of all expressed and DESeq2-tested genes. Gene set enrichment analyses (GSEA) were performed following developer's instructions (https://www.gsea-msigdb.org/) with signal2Noise metric and 1000 permutations as previously described[95]. RNA-sequencing data is available at the Gene Expression Omnibus (GEO) under the accession number GSE322665.

Please cite this article in press as: Xavier et al., Programmed ribosomal frameshifting triggers translational stress to promote viral replication, Cell (2026), https://doi.org/10.1016/j.cell.2026.08.031

RT-qPCR

Reverse transcription reaction was performed using 1μg of isolated total RNA, random hexamer primer and ProtoScript II Reverse Transcriptase (NEB). Synthesized cDNAs were further diluted 10-fold in water and 1μl was used for each qPCR reaction. qPCR was performed using 2X SyberGreen mix (Takyon) and LightCycler (BioRad). C_t values were obtained and normalized by those of a housekeeping gene (Gapdh). The results were quantified by $2^{-\Delta\Delta C}{}_T$ method. Melting curves confirmed the quality of each primer. +

Disome RT-qpcr

RNA from disome fractions of RNase I digested Polysome profile experiments was purified from TriZOL by equilibrating at RT for 15min and adding 200 μl chloroform followed by vortexing for 15 sec. Tubes were incubated for 3 min at RT followed by 15 min centrifugation at 15000 RPM in an Eppendorf tabletop centrifuge at 4°C. The aqueous phase was removed from the top and transferred to Quiagen RNeasy kit columns and processed according to manufacturer's instructions. Qpcr primers were designed from GenBank: OX368027.1 nt 13409–13478 with a product size of 69 bp. Specific amplification was assessed through melting curves and agarose gel analysis of the qpcr product.

MS2 pulldown assay

HEK cells were co-transfected in 15 cm dishes with a construct transcribing N-terminal MS2 loops followed by minimal pseudoknot region of SARS-CoV-2 WT (GenBank: OX368027.1 nt 13016-13989) or ΔL1 (ΔT13485-C13487) mutant and a construct expressing GFP-MS2CP (addgene # 27121). 48h post transfection, cells were harvested in RNA/DNA lobind tubes and lysed in lysis buffer A (20 mM TRIS pH 7.5, 150 mM NaCl, 1.5 mM MgCl2, 1 mM DTT,0,5% NP-40, 1 mini complete protease inhibitor, EDTA-free, RNAse free) and incubated with GFP-trap agarose (chromotec) for 16h followed by 3 washes with wash buffer B (20 mM TRIS pH 7.5, 300 mM NaCl, 1.5 mM MgCl2, 1 mM DTT) and 1 wash with lysis buffer. Beads were boiled in 1x SDS sample buffer for 10 min and loaded on SDS PAGE, followed by western blotting.

RIP-qPCR assay

GCN2 KD (1-1040 AA) and GCN2 HRS (1025-1649AA) and GCN2 FL (1-1649AA) were cloned into pcDNA 3.1 with a C-terminal myc-DDK tag. HEK cells were co-transfected with GCN2 KD or HRS and ctrl/FS MS2loop construct for 48h and lysed in RNAse free lysis buffer A followed by incubation with 15 μg of c-myc antibody (santa cruz 9E10-sc-40) over night and coupled with IgG beads for 1h at 4°C. Beads were washed 3 times in wash buffer B followed by 1 wash with buffer A. Beads were dissolved in 1 mL TRiZOL and frozen at -20°C over night. RNA was purified from TRiZOL by equilibrating at RT for 15min and adding 200 μl chloroform followed by vortexing for 15 sec. Tubes were incubated for 3 min at RT followed by 15 min centrifugation at 15000 RPM in an Eppendorf table top centrifuge at 4°C. The aqueous phase was removed from the top and transferred to Quiagen RNeasy kit columns and processed according to manufacturer's instructions. RT-qPCR was performed as described above.

In vitro translation and GCN2 kinase assay

For *in vitro* transcription and translation we made minimal frameshifting constructs containing only the minimal frameshifting site in pcDNA 3.1 (CGCCGGTCCGTAACCCACCGTATTCTTACCGTTCCGATTGCCCAAGATCAAGTGGGCGCATACTATCAGCAACCAGG TCAGCAGAACGCCACCTGGATTGTGCCACCAGGGCCAACTTGTGCTAATGACCCTGTGGGTTTTACACTTAAAAACACAGTCTGTA CCGTCTGCGGTATGTGGAAAGGTTATGGCTGTAGTTGTGATCAACTCCGCGAACCCATGCTTCAGTCAGCTGATGCACAATCGTTT TTAAACGGGTTTGCGGTGTAAGTGCAGCCCGTCTTACACCGTGCGGCACAGGCACTAGTACTGATGTCGTATACAGGGCTTTTGA CATCTACAATGATAAAGTAGCTGGTTTTGCTAAATTCCTAAAAACTAATTGTTGTCGCTTCCAAGAAAAGGACGAAGATGACAATTTA ATTGATTCTTACTTTGTAGTTAAGAGACACACTTTCTCTAACTACCAACATGAAGAAACAATTTATAATTTACTTAA) with corresponding mutations (see above). *In vitro* transcription was performed using MEGAscript™ T7 high yield transcription kit from Thermofisher scientific according to manufacturer's instructions. GCN2 kinase assay was performed using nuclease treated rabbit reticulocyte lysate system from Promega. 1μg RNA (FS/ctrl) and 100 nM GCN2 FL were added to rabbit reticulocyte lysate for 30 min at 37°C. EIF2α phosphorylation was detected using western blot with anti p-eIF2α antibody). For translation inhibition rabbit reticulocyte lysate was pre-treated with 100 mg/l cycloheximide for 15 min prior to adding RNA and GCN2 FL.

Puromycin incorporation assay

Calu-3 cells were treated with 3 μM A92 followed by infection with SARS-CoV-2 as described below at multiplicity of infection (MOI) 1 for 10h. Treatment of non-infected Calu-3 cells with 100 μg/ml CHX for 10 min served as negative control. HEK293T cells were transfected with ΔL1, FS or Flag-Nsp1 for 48h. Following incubation time, cells were treated with 10 μg/mL puromycin for 10 min, washed quickly with 1x DPBS and lysed or frozen immediately for western blotting.

Recombinant protein purification GCN2 insect cell expression and purification

Recombinant baculovirus encoding full length human GCN2 with N-terminal TEV-cleavable 6xHis-StrepII-tag was gifted from Glenn Masson MRC, Dundee, UK.Virus was propagated in TriX Sf9 insect cells (RRID: CVCL_0549). For protein expression, 9.6 L exponentially growing cells (2 x 106 cells/mL), cultured in Lonza Insect-Xpress medium (Lonza RRID:SCR_000377, BELN12-730), were infected with high-titre baculovirus suspension. Cells were incubated for 66 h shaking with 90 rpm at 27°C for protein expression

and harvested by centrifugation. Cell pellets were washed with phosphate buffered saline (PBS) and frozen at -20°C. For protein purification, cell pellets were thawed and resuspended in lysis buffer (50 mM HEPES pH 7.4, 500 mM NaCl, 20 mM imidazole, 0.5 mM TCEP, 5% glycerol). All steps were performed on ice. Lysis was carried out by three rounds of sonication (35% amplitude, 5 sec pulse, 10 sec pause, 3 min pulse time). The lysate was cleared by ultracentrifugation for 60 min 100 000xg at 4°C. Clarified lysate was loaded onto pre-equilibrated Ni-NTA sepharose (Qiagen, 30250). After washing with lysis buffer, 6xHis-tagged protein was eluted in lysis buffer supplemented with 300 mM imidazole. The eluate was further subjected to a pre-equilibrated StrepTrap XT column (Cytiva, 29401322) using an AKTA start protein purification system (Cytiva). After washing, the protein was eluted using elution buffer (50 mM HEPES pH 7.4, 500 mM NaCl, 50 mM biotin, 0.5 mM TCEP, 5% glycerol). Protein containing fractions were pooled and treated with TEV protease overnight at 4°C to cleave the 6xHis-StrepII-tag. Contaminating proteins, cleaved tag, uncleaved protein and TEV protease were removed by performing a Ni-NTA rebinding. Finally, GCN2 was concentrated and subjected to gel filtration in 20 mM HEPES pH 7.4, 150 mM NaCl, 0.5 mM TCEP, 5% glycerol, 2.5 mM MgCl2 using an AKTA Xpress system combined with a S200 16/200 column (GE Healthcare). The elution volume 56.5 mL indicated the protein to be monomeric in solution.

Virus propagation and infection

For SARS-CoV-2 propagation Caco-2 cells were used as previously described.[96] Viral titers were determined by Tissue Culture Infection Dose 50 ($TCID_{50}$) and virus aliquots stored at -80 °C. In this study, the SARS-CoV-2 variant B.1 (FFM7/2020; MT358643[96]) was used for all main experiments and the Delta B.1.617.2 (FFM-IND8424/2020; MZ31514),[97] Omicron BA.1/B.1.1.529a (2021; EPI_ISL_6959868)[98] and Omicron JN.1 variant for verification. WNV strain NY385-99 was propagated on Vero cells as previously described and kindly provided by Dr. J. ter Meulen (Institut für Virologie, Phillips-Universität Marburg, Germany).[99] Viral titers were determined by Tissue Culture Infection Dose 50 ($TCID_{50}$) and virus aliquots stored at -80 °C. HIV-1 NL4-3 virus stock were generated as described elsewhere.[100,101] Briefly, by transfection of HEK293T cells with pNL4-3. 24 h post-transfection the media was changed to IMDM (Gibco) supplemented with 10% (v/v) heat-inactivated fetal calf serum (FCS) and 50 μg/ml of penicillin and streptomycin (P/S) each (Invitrogen). 48 h post-transfection the supernatant was collected, centrifuged at 500 x g and 4 °C for 10 min and filtrated through a 0.45 μM low-binding filter unit (Merck) and virus aliquots were stored at -80 C. $8.8x10^5$ Jurkat cells were seeded per well in 12-well plates and treated with 0.375 μM or 0.75 μM A92 or DMSO as solvent control. After 1 h the cells were infected with HIV-1 NL4-3 at an MOI (multiplicity of infection) of 1. At 0, 18, 24, 36 and 48 h post infection, the supernatant was collected and the cells were washed with PBS and lysed with RIPA buffer containing cOmplete protease inhibitor cocktail (Roche). Lysates were subjected to a freeze-thaw cycle at -20 °C before further use.

For virus infection Calu-3 or A549 A+T (for SARS-CoV-2) or ARPE-19 (for WNV) cells were washed with 1x PBS and supplemented with 1% FCS cell culture medium. Virus inoculum at indicated MOI was incubated for 2 hours and subsequently substituted with fresh 1% FCS medium. ALI HBE cultures were washed three times with PBS and inoculated with SARS-CoV-2 at indicated MOI for 2 h from the apical side. After the incubation period, inoculum was removed, and cells were washed three times with PBS. For drug testing, ALI HBE cultures were pretreated with A92 for one hour followed by treatment and simultaneous infection for two hours (three hours drug treatment in total). After the incubation period, virus was inactivated with previously described validated methods.[102] Briefly, for western blot samples, Cells were lysed directly in WB lysis buffer (20 mM TRIS/HCl pH 7.5, 150 mM NaCl, 10 mM NaPPi, 20 mM NaF, 1% Triton X-100, 1.9 M glycine, and 250 mM TRIS base) supplemented with cOmplete™ protease inhibitor cocktail (Roche). Following sample preparation, lysates were heated in Laemmli buffer for 10 min at 90°C. For RT-qPCR samples, Virus was inactivated by adding AVL lysis buffer according to the Qiagen RNA isolation kit protocol prior to RNA extraction.

Nanopore GridION Sequencing

Cell culture SARS-CoV-2 virus isolate was subjected to whole genome sequencing on the Oxford Nanopore GridION™ (Oxford Nanopore Technologies, Oxford, UK) using 1,200 bp amplicon rapid sequencing[103] using Midnight Amplicon Panel v2 primers (Integrated DNA Technologies, Leuven, Belgium). The SARS-CoV-2 consensus genome was generated by processing the Fastq files generated from sequencing with the EPI2ME Labs ARTIC SARS-CoV-2 workflow[104] and deposited in GISAID.[105] The SARS-CoV-2 variant and lineage was determined using the Nextclade app[106] with the consensus sequence.

TZM-bl Luc Assay

TZM-bl cells harbor a luciferase and β-galactosidase expression cassette under the control of the HIV-1 LTR promoter, which is activated in infected cells due to the expression of the HIV-1 trans-activator of transcription (Tat). TZM-bl cells were seeded at a density of $4x10^4$ cells per well in 96-well plates in 100 μl cultivation media and incubated overnight at 37 °C and 5% CO_2. 100 μl of the viral supernatant and successive dilutions were added to the cells and incubated for 48 h. The cells were washed with PBS and then lysed with 120 μl of lysis juice (p.j.k) for 15 min at room temperature. Cells were subjected to a freeze-thaw cycle at -80 °C prior to measurement. Lysates were resuspended and 30 μl were transferred to a white microplate (Costar) for luminescence readout. 120 μl of beetle juice (p.j.k) was added per well and luminescence was measured using the GloMax Discover (Promega) with an integration time of 5 s. Protein levels were determined by using the Pierce™ Bradford assay kit (Thermo Scientific™) according to the manufacturer's instructions and used for normalization.

Please cite this article in press as: Xavier et al., Programmed ribosomal frameshifting triggers translational stress to promote viral replication, Cell (2026), https://doi.org/10.1016/j.cell.2026.08.031

TZM-bl x-Gal Assay

TZM-bl cells were seeded at a density of $5x10^3$ per well in 96-well plates in 100 μl cultivation media and incubated overnight at 37 °C and 5% CO_2. 100 μl of viral supernatant and successive dilutions were added to the cells and incubated for 48 h. The cells were washed with cold PBS and fixed with PBS containing 0.25% Glutaraldehyde and 0.9% Formaldehyde for 15 min at 4 °C. The fixed cells were washed with cold PBS and stained with a solution containing 4 mM potassium ferricyanide ($K_3[Fe(CN)_6]$), 4 mM potassium ferrocyanide ($K_4[Fe(CN)_6]$), 8 mM magnesium chloride ($MgCl_2$), and 0.8 mg/ml X-Gal. Following overnight incubation at 37 °C, cells were overlayed with 50% glycerol. Readout was performed optically with light microscopy. Brightfield images were taken using the SparkCyto plate reader (Tecan).

Transepithelial electrical resistance (TEER) measurement

Prior to measurement, ALI HBE cultures were supplied with medium on their apical side for 30 min. TEER values were determined by a chopstick electrode connected to a Volt-Ohm-meter (Millicell® ERS-2, Merck) according to the manufacturer's instructions.

Antiviral and viability assay

Confluent Calu-3 or ARPE-19 cells were treated with the GCN2 Inhibitor GCN2-IN-1/A92 (MedChemExpress #HY-100877) diluted in 1 % FCS cell culture medium. Cells were transfected with 20μM siRNA 24h prior to infection. Cells were either incubated for 24 hours to access cell viability or infected with SARS-CoV-2 at an MOI of 0.02 (Calu-3) or WNV at an MOI of 0.2 (ARPE-19) for 24 hours. Antiviral effects were evaluated using immunofluorescence imaging. For determining cell viability, 25 μl of 3-(4,5-dimethylthiazol-2-yl)-2,5-diphenyltetrazolium bromide (MTT) solution (2 mg/ml) were added per well and incubated for 3 h at 37 °C followed by 100 μl of lysis buffer (20% SDS and 50% N,N-dimethylformamide, pH 4.7) over night at 37 °C. Absorbance was measured at 560/620 nm with a Tecan infinite M200 microplate reader (TECAN). The 50 % cytotoxicity concentration (CC50) and 50 % inhibitory concentration (IC50) were calculated with nonlinear regression using Graph Pad Prism (GraphPad Software).

Immunofluorescence

SARS-CoV-2 infected Calu-3 cells were fixed with ROTI®Histofix (Roth) for 20 min followed by permeabilisation with 0.5 % Triton-X for 20 min. Unspecific binding sites were blocked with 1 % bovine serum albumin (BSA) for 1 h. WNV infected ARPE-19 cells were fixed and permeabilized with acetone:methanol (40:60) for 30 min followed by incubation with blocking solution (BS; 2 % BSA, 5 % goat serum, 0.01 % Thimerosal) for 1 h at 37°C. Primary antibody was incubated over night at 4 °C. After washing four times with 1 x PBS, secondary antibody mixed with DAPI (0.02 mg/ml) was incubated for 1 h at room temperature and 10 rpm followed by four washings steps with 1 x PBS. Antibodies used were as followed: rabbit anti SARS-CoV-2 Spike (Sino Biological #40150-R007 1:1000, 0.5 % BSA), goat anti rabbit Alexa 488 (Invitrogen # A11008 1:1000, 0.5 % BSA), Flavivirus E-protein (Merck #MAB10216-I 1:2000, BS), goat anti mouse Alexa 647 (Invitrogen #A21235, 1:1000, PBS). Image acquisition and analysis were performed with the Operetta CLS High Content Analysis System (PerkinElmer) and the corresponding Software Harmony (PerkinElmer).

Detection of extracellular viral RNA

Apical washes from ALI HBE cultures were used to determine extracellular SARS-CoV-2 levels. Virus was inactivated by ACL buffer supplemented with carrier RNA and Proteinase K (all from QIAGEN) followed by incubation at 56 °C for 30 min. Isolation of viral RNA was performed with the QIAamp 96 Virus QIAcube HT Kit (QIAGEN) according to the manufacturer's instructions. The Luna Universal ONE-Step RT qPCR Kit (New England Biolabs) was applied for quantitative PCR using a CFX96 Real-Time System (Bio-Rad). The following primers were adapted from the WHO: SARS-CoV-2 RNA-dependent RNA polymerase (RdRp): RdRP_SARSr-F2 (GTGARATGGTCATGTGTGGCGG), RdRP_SARSr-R1 (CARATGTTAAASACACTATTAGCATA). For determining viral copy numbers, a standard row using the plasmid pEX-A128-RdRP that contains the corresponding amplicon (see GenBank accession number NC_045512) was created.

siRNA-mediated knockdown

Calu-3 cells were seeded in 96-well plates or 12-well plates to be 60-80 % confluent at the time of transfection. siRNA and Lipofectamine RNAiMAX (Thermo Fischer Scientific #13778075) were diluted in Opti-MEM (Gibco), mixed in a 1:1 ratio and incubated at RT for 5 minutes. The final siRNA concentrations were 40 nM and final Lipofectamine RNAiMAX volumes 0.16 μl and 1.8 μl per well for 96-well and 12-well, respectively. After 48 hours, cells were infected followed by assessment of virus inhibition via immunofluorescence and knock down verification via immunoblot.

$3x10^5$ HEK293T cells were seeded in 6-well plates coated with Poly-L-Lysine (Sigma) in culture media. 24 h post seeding, cells were transfected with 1 μg pNL4-3 and siRNAs with a final concentration of 40 nM and final Lipofectamine 2000 (Thermo Fisher Scientific) of 5 μl per well. After 72 h, cells were lysed with RIPA buffer and supernatant was collected for further analyzation.

Polysome profiling

Confluent T-175 flasks of Calu-3 cells were washed, supplemented with 1% FCS cell culture medium and either treated with DMSO or 3 μM GCN2 Inhibitor GCN2-IN-1/A92. After 1 hour of incubation, cells were infected with SARS-CoV-2 B.1 at an MOI of 0.2. At different time points post infection (0 h, 4 h, 10 h, 24 h), cells were washed with and scraped into ice-cold 1 x DPBS supplemented

with calcium and magnesium (Gibco #14040117) followed by centrifugation at 1,200 xg for 4 min at 4 °C. For HEK293T experiments cells were transfected with ΔL1 or FS SARS constructs for 48h and harvested under the same conditions as Calu-3 cells. Cell pellets were resuspended in 220 μl polysome buffer (25 mM HEPES pH=7.5, 100 mM NaCl, 10 mM MgCl2, 2 mM dithiothreitol (DTT), Complete EDTA-free protease inhibitor cocktail (Millipore Sigma #COEDTAF-RO). Triton X-100 and sodium deoxycholate were added to a final concentration of 1% each and the samples were incubated on ice for 20 min and centrifuged at 20,000 xg for 10 min at 4 °C. 250 μl of supernatants were flash frozen and stored at -80 °C. Frozen samples were thawed on ice, RNA concentrations were measured using Qubit and 200μg RNA loaded on top of 10-50% or 100 μg (prior to RNase I digestion) on top of 15-30% sucrose density gradients (approx. 11 mL) in polysome buffer. For lysates for nuclease resistant disome analysis, 100 μg lysate was digested using 7.5 μl of RNase I (100 U/μL) for 45 min and quenched with 10 μl SUPERaseIn (20 U/μl). These linear gradients were prepared the day of in thin-wall polypropylene tubes (Beckman Coulter, 331372) using a gradient maker (Gradient Master 108 (BioComp)) and stored at 4 °C until use. Gradients were subjected to ultracentrifugation at 36,000 rpm (222,200 x *g*) in a SW41-Ti rotor (Beckman Coulter) for 2 hours 30 min at 4 °C. Gradients were then run at 1.5 mL/min in a density gradient fractionation system (Teledyne Isco), followed by a chase of 60% sucrose and 10% glycerol in water, with continuous monitoring at 254 nm using a UA-6 absorbance detector. Approximately 15 equal-volume fractions were collected every 30 seconds using a Foxy R1 fraction collector (Teledyne Isco), then flash frozen and stored at -80°C until further analysis. The area under the curve (AUC) of individual absorbance peaks was measured using a custom web-based application developed with R Shiny, which calculates the AUC based on user-defined points through a manual integration method. For each polysome profile, the monosome/polysome ratio was calculated as the AUC of the monosome peak divided by the combined AUC of all polysome peaks. For the comparison of different treatments, multiple polysome profiles were aligned to the monosome peak.

UV-treatment and glutamine starvation

For UV-treatment, HEK293T plated on 6-well plates transfected with siRNA for 48h and exposed to 1200 m/J^2 with the lid off. Afterwards cells were recovered at 37°C with 5%CO_2 for 0,60 or 120 min and harvested as stated above. For glutamine starvation HEK293T cells were plated on 6-well plates transfected with siRNA for 48h and washed with DMEM medium lacking glutamine twice. Cells were starved in DMED lacking glutamine for 2h before harvesting for western blotting.

Mass spectrometry sample preparation

The samples were denatured at 95 °C in the presence of 10 mM TCEP and 40 mM CAA. Proteins were precipitated using methanol-chloroform and resuspended in 8 M urea, 50 mM Tris pH 8.5. Afterwards, proteins were digested with 1:50 w/w LysC (Wako Chemicals, cleaves at the carboxylic side of lysine residue) and 1:100 w/w trypsin (Promega, Sequencing-grade) overnight at 37 °C after dilution to a final urea concentration of 1 M using 50 mM Tris pH 8.5. Digested peptides were then acidified (pH 2–3) using trifluoroacetic acid (TFA) and purified using C18 SepPak columns (Waters). Desalted peptides were dried and resuspended in 3% ACN, 0.1% TFA for label-free LC-MS analysis.

Mass spectrometry data acquisition

Tryptic peptides were analyzed on an Orbitrap Lumos coupled to an easy nLC 1200 (ThermoFisher Scientific) using a 35 cm long, 75 μm ID fused-silica column packed in house with 1.9 μm C18 particles (Reprosil pur, Dr. Maisch), and kept at 50 °C using an integrated column oven (Sonation). HPLC solvents consisted of 0.1% Formic acid in water (Buffer A) and 0.1% Formic acid, 80% acetonitrile in water (Buffer B). Peptides were eluted by a non-linear gradient from 4-40% acetonitrile over 60 minutes and directly sprayed into the mass-spectrometer equipped with a nanoFlex ion source (ThermoFisher Scientific). Full scan MS spectra (300-1500 m/z) were acquired in Profile mode at a resolution of 60,000 at m/z 200, a maximum injection time of 50 ms and an AGC target value of $4x10^5$. Up to 10 most intense peptides per full scan were isolated using a 1.4 Th window and fragmented using higher energy collisional dissociation (normalised collision energy of 30). MS/MS spectra were acquired in centroid mode with a resolution of 15,000, a maximum injection time of 22 ms and an AGC target value of $1x10^5$. Single charged ions, ions with a charge state above 6 and ions with unassigned charge states were not considered for fragmentation and dynamic exclusion was set to 45 s.

Mass spectrometry data analysis

MS raw data were analyzed using FragPipe v21.1, with MSFragger v.4.0[92] and Philosopher v.5.1.0.[89] Acquired spectra were searched against the human reference proteome (Taxonomy ID 9606) downloaded from UniProt (07/25/2024; 20,418 entries) with a precursor mass tolerance of 20 ppm and fragment mass tolerance of 20 ppm. Identifications were filtered to obtain false discovery rates (FDR) below 1% for both peptide spectrum matches (minimum peptide length of 7) and proteins using a target-decoy strategy. For all searches, carbamidomethylated cysteine was set as a fixed modification and oxidation of methionine and N-terminal protein acetylation as variable modifications with allowing up to 3 modifications per peptide. Strict trypsin cleavage was set as protein digestion rule. Label-free quantification was performed using IonQuant v.1.10.27.[90] Data were further processed using FragPipe Analyst.[91]

Ribo-seq

Confluent T-175 flasks of Calu-3 cells were washed, supplemented with 1% FCS cell culture medium and either treated with DMSO or 3 μM GCN2 Inhibitor GCN2-IN-1/A92. After 1 hour of incubation, cells were infected with SARS-CoV-2 B.1 at an MOI of 0.2. At 24 h

post infection cells were washed with and scraped into ice-cold 1 x DPBS supplemented with calcium and magnesium (Gibco #14040117) followed by centrifugation at 1,200 xg for 4 min at 4 °C. Cells were lysed in ice-cold lysis buffer (25 mM Tris-HCl pH 7.5, 150 mM NaCl, 10 mM MgCl2, 1% Triton-X, 1% sodium deoxycholate, 2 mM DTT) and incubated on ice for 10 min. Lysates were clarified at 12,000 rcf for 5 min at 4°C. 5 μl RNase I (Invitrogen) was added to 200 μl of lysate and incubated at RT for 45 min. Digested lysates were filtered through MicroSpin S-400 HR columns (Cytiva) at 600 x rcf for 2 min at 4°C and eluates containing ribosome protected fragments were extracted with 4:1 v/v TRIzol™.

Ribo-seq analysis

Ribosome profiling (ribo-seq) cDNA libraries were prepared essentially as described.[75] Briefly, ribosome protected fragments were size selected, linker ligated, circularized, and PCR amplified for Illumina sequencing. Below are details of the experimental procedure. Ribosome protected fragments were separated by homemade denaturing 15% UREA-PAGE and visualized by SYBR Gold (Thermo). RNA in the size range of 25-35 nt was excised from the gel and eluted in 300 μl RNA extraction buffer (300 mM NaOAc pH 5.5, 1.0 mM EDTA, 0.25% SDS) at 22 °C overnight using a Thermomixer with shaking at 500 rpm. Extraction solution was transferred to fresh tubes and combined with 1.5 μL Pellet Paint (EMD Millipore) 450 μL isopropanol. After overnight at -80 °C, RNA was pelleted for 30 min in a tabletop microfuge at 20,000 xg, 4 °C. Supernatant was replaced with 500 μl ice-cold 75% ethanol, followed by another spin at 7500 xg, 4 °C, for 5 min. Pellets were air dried, resuspended in 17 μl nuclease-free water, and transferred to PCR tubes. For the dephosphorylation-ligation reaction, 17 μl of RNA was combined with 2 μl 10X T4 PNK buffer, 1 μl Superase-In (Thermo) and 0.5 μl T4 PNK (NEB). Reactions were incubated at 37 °C for 30 min and 65 °C for 20 min. Next, the reactions were supplemented with 4.5 μl DMSO, 6 μl 50% PEG400 (Thermo), 3.5 μl 10X T4 RNA ligase buffer (NEB), 1 μl T4 RNA Ligase 2 (NEB) and 1 μl 20 μM pre-adenylated rApp-L7. Content was moved to eppendorf tubes and incubated at 16 °C overnight using a Thermomixer with shaking at 500 rpm. This was followed by 1 h incubation at 37 °C and 15 min at 65 °C. 20 μl MyONE Silane beads (Thermo) were combined with 650 μl RLT buffer (Qiagen) and added to the ligation reactions. 720 μl 100% ethanol was added and mixed gently by pipetting. Incubated for 5 min at room temperature followed by another gentle pipetting and 5 min incubation at room temperature. Using a magnetic rack, supernatant was discarded, and beads were washed 3x in 1 mL ice-cold 75% ethanol and air dried at room temperature. The final wash was removed, and beads were resuspended in 12 μl nuclease-free water. Incubated for 5 min at room temperature and replaced on the magnetic rack. Supernatants were transferred to fresh tubes and supplemented with 0.5 pmol P7 reverse-transcription (RT) oligonucleotide and 1 μl 10 mM dNTP mix and incubated at 70 °C for 5 min followed by quick cooling. Then, supplemented with 4 μl 5x SuperScript III First Strand buffer (Thermo), 1 μl 0.1 M DTT, 0.5 μl Superscript III RT and 1 μl Superase-In, and incubated at 25 °C for 5 min, 42 °C for 20 min, 50 °C for 40 min, 80 °C for 5 min. To hydrolyze the RNA, 1.65 μl 1 M NaOH was added and reactions were incubated at 90 °C for 20 min, followed by neutralization using 20 μl 1 M HEPES pH 7.3. 20 μl MyONE Silane beads were combined with 650 μl RLT buffer and added to the samples. 720 μl 100% ethanol was added and gently mixed by pipetting. Incubated for 5 min at room temperature followed by another gentle pipetting and 5 min incubation at room temperature. Using a magnetic rack, supernatant was discarded and beads were washed 3x in 1 mL ice-cold 75% ethanol and air dried at room temperature. Beads were resuspended in 15 μl nuclease-free water, incubated for 5 min at room temperature, and the supernatant was transferred to PCR tubes using magnetic beads. For circularization, samples were supplemented with 2 μl 10X CircLigase buffer (Lucigen), 1 μl 1 mM ATP, 1 μl 50 mM $MnCl_2$, 1 μl CircLigase enzyme and incubated for 2 h at 60 °C, followed by 10 min at 80 °C. 10 μl MyONE Silane beads were combined with 650 μl RLT buffer and added to the samples. 720 μl 100% ethanol was added and gently mixed by pipetting. Incubated for 5 min at room temperature followed by another gentle pipetting and 5 min incubation at room temperature. Using a magnetic rack, supernatant was discarded and beads were washed 3x in 1 mL ice-cold 75% ethanol and air dried at room temperature. Beads were resuspended in 23 μl nuclease-free water and incubated for 5 min at room temperature. Supernatants were removed to fresh tubes for rRNA depletion and supplemented with 1 μl rRNA substraction oligo pool[76] and 2.6 μl 20X SSC and incubated in a thermocycler for 90 sec at 100 °C followed by slow cooling at -0.1 °C/sec down to 37 °C. Using a magnetic rack, wash 25 μl MyOne Streptavidin C1 DynaBeads (Thermo) x3 in 25 μl 1x Bind/Wash buffer (1 M NaCl, 0.5 mM EDTA, 2.5 mM Tris pH 7.5 and 0.1% Triton X-100). Resuspended in 12.5 μl 2x Bind/Wash buffer and transfer 10 μl of beads into fresh tubes and equilibrate at 37 °C. Add 17 μl 2x Bind/Wash buffer and 27 μl of reaction mixture and incubate for 15 min at 37 °C, with shaking at 1000 rpm. Using a magnetic rack, 52 μl of each supernatant was removed into fresh tubes, supplemented with 1.5 μl Pellet Paint, 6 μl 5 M NaCl and 74 °C nuclease-free water. The reactions were vortexed, combined with 200 μl isopropanol, and left overnight at -20 °C. Nucleic acid was precipitated in a tabletop microfuge at 20,000 xg for 30 min at 4 °C. Pellets were washed with 500 μl ice-cold ethanol followed by another spin at 7500 xg for 5 min at 4 °C. Pellets were air dried and resuspended in 22 μl nuclease-free water. PCR pre-amplification was performed using P5_s and P7_s oligonucleotides. 22 μl circularized RT products were combined with 3 μl 10 μM P5Solexa_*s and P7Solexa_*s and 25 μl 2X KAPA HiFi Hot Start (Roche) and incubated in a thermocycler as follows: 6 cycles of 95 °C for 3 min, 98 °C for 20 sec, 65 °C for 15 sec, 72 °C for 30 sec and 72 °C for 1 min. Each 50 μl sample was then supplemented with 147.5 μl ProNex beads (Promega) and incubated for 10 min at room temperature. Using a magnetic rack, the supernatant was replaced with 300 μl ProNex Wash Buffer and incubated for 30-60 sec. After another identical wash, the beads were air dried for about 10 min, removed from the magnetic stand and combined with 23 μl ProNex Elution Buffer. Eluted cDNA was transferred to fresh tubes. Scouting PCR was performed using 3.4 μl nuclease-free water, 0.3 μl 10 μM P5 Solexa Primer, 0.3 μl 10 μM TruSeq P7 Index Primer, 1 μl cDNA and 5 μl 2x KAPA HiFi Hot Start mix. Reactions were amplified for 6 or 9 cycles, as follows: 95 °C for 3 min, 98 °C for 20 sec, 65 °C for 15 sec, 72 °C for 30 sec, 72 °C for 1 min. Reaction products were visualized using a 1% agarose gel and SYBR safe

dye. For the final PCR, 10 μl cDNA was combined with 8.8 μl nuclease-free water, 1.2 μl 10 μM P5Solexa and TruSeq P7 Index primer mix and 20 μl 2x KAPA HiFi Hot Start mix. Amplification was performed as follows: 95 °C for 3 min, 98 °C for 20 sec, 65 °C for 15 sec, 72 °C for 30 sec and 72 °C for 1 min, for 3-6 cycles (based on scouting PCR). Reactions were supplemented with water up to 100 μl and combined with 1.5 μl Pellet Pain and 175 μl isopropanol. Libraries were pelleted in a tabletop microfuge at 20,000 xg, 4 °C, followed by wash with 500 μl ice-cold 75% ethanol and another spin at 7500 xg for 5 min at 4 °C. Pellets were air dried, resuspended in 10 μl water. PCR products were resolved on an 8% native PAGE, visualized using SYBR Gold and extracted in 200 μl DNA extraction buffer (300 mM NaCl, 10 mM Tris pH 8, 1 mM EDTA). Extractions were frozen at -80 °C and then tumbled overnight at room temperature. Supernatants were removed to fresh tubes, pelleted as above and resuspended in 15 μl water. Library concentration was determined using a TapeStation, pooled, and submitted to single-read sequencing on NovaSeq X 1.5B. Reads were demultiplexed, adaptors (AGATCGGAAGAGCACACGTCT) were removed using cutadapt and the first 7 and last 3 nt were removed using Trim Galore. Reads mapping to human ribosomal RNA sequences were removed using HISAT2 and unaligned sequences were searched again against the human hg38 genome, both using default parameters. FeatureCounts was used to quantify 28-32 nt reads mapping to exons, and count tables were median adjusted and filtered for coding genes using UniProt 9606 Human Proteome. Then, differential expression analysis was performed on Mock and CoV2 samples (Student's t-test FDR<0.05. S0=0.1). The dataset was filtered for transcripts with statistically significant differences, and this subset was z-scored and subjected to unsupervised hierarchical clustering with k-means

Generation of SARS-CoV2 replicon reporter system

SARS-CoV-2 isolate USA-WA1/2020 was used to clone the full-length SARS-CoV-2 genome into a BAC plasmid using NEBuilder HiFi Cloning kit (NEB). In this pCMV-SARS-CoV-2 plasmid, the viral genome was placed under the control of a CMV promoter. The viral 3'UTR was followed by a 22 base-long polyA tail, a hammerhead ribozyme and a bovine growth hormone (BGH) polyadenylation signal in order to facilitate nuclear export of SARS-CoV-2 viral RNA and the self-cleaving of the heterologous BGH polyadenylation signal to obtain a full-length viral RNA genome in the cytoplasm. SARS-CoV-2 replicon reporter was generated by digesting the pCMV-SARS-CoV-2 plasmid with SphI to remove the Spike ORF and replace it with a fusion reporter composed of eGFP and NanoLuciferase. The other viral accessory ORFsand structural viral genes (E, M and N) were reintroduced at the same time. Replicon-dependent activity of the reporter was confirmed by inhibition of its activity following treatment with the viral replication inhibitor Molnupiravir (Cayman Chemical).

Programmed Ribosomal Frameshift (PRF) mutants between ORF1a and ORF1b were introduced by digesting the replicon reporter plasmid with PmeI and Bsu36I to remove a ORF1ab region containing the PRF sequence and reintroducing it with two overlapping PCR product bearing either mutation (ΔL1 and mut1).

All constructs were confirmed by full plasmid sequencing (Plasmidsaurus).

QUANTIFICATION AND STATISTICAL ANALYSIS

The details of experiments including the statistical tests used, sample size are indicated in method details, figures, and figure legends. Graphpad Prism was used for statistical analyses if not specified otherwise.